Solid Propellant Microrockets

by Dana Teasdale

Research Project

Submitted to the Department of Electrical Engineering and Computer Sciences, University of California at Berkeley, in partial satisfaction of the requirements for the degree of **Master of Science, Plan II**.

Approval for the Report and Comprehensive Examination:

Committee:

Professor Kristofer S. J. Pister
Research Advisor

19 May 2000

* * * * * * *

Professor Albert P. Pisano
Second Reader

19 May 2000

Abstract

This paper details the design, fabrication and testing of millimeter scale solid propellant rockets for use as one-time deployment platforms carrying communication-equipped MEMS sensor systems, known as Smart Dust. Each rocket assembly is an integrated system, incorporating a combustion chamber, composite propellant grain, nozzle, igniter, and thermoelectric power converter. Solid propellant is advantageous for a millimeter-scale single-use device because of its simple implementation, unlike liquid propellants, which require a more elaborate system of pumps and valves. Therefore, the total system volume and complexity are minimized.

Combustion chambers were fabricated in various materials, including silicon wafers; however, thermal losses were too high to reliably maintain a burn. Therefore, cylindrical alumina ceramic combustion chambers with thermal conductivities five times lower than silicon are used. Thrusts of up to15 mN have been measured for ceramic rockets weighing under 1 g, with specific impulses in the 10 to 20 s range. By reducing the propellant mass fraction and optimizing the nozzle geometry, calculations show that flight producing thrusts can be generated.

Silicon nozzles integrated with polysilicon igniters and thermopiles for thermal power conversion have been microfabricated in a single process. Fuel ignition by polysilicon heaters suspended on a low-stress nitride (LSN) membrane has been demonstrated. Igniters require as little as 0.2 W to ignite composite propellant, primarily composed of hydroxyl-terminated polybutadiene (HTPB) and ammonium perchlorate (AP). The igniter is suspended for thermal isolation through bulk post-processing by a backside deep reactive ion etch (DRIE). The etched hole beneath the igniter also serves as a nozzle through which high-velocity combustion gases exit the rocket. Thermopiles, which generate voltages proportional to hot and cold junction temperature differentials, have been fabricated in the same process as igniters, and span backside DRIE thermal isolation cavities. With potential temperature differences of hundreds of degrees and a total of 120 thermocouple junctions fabricated on the silicon nozzle chip, hundreds of milliwatts of power could feasibly be produced during the microrocket's flight and used to power Smart Dust circuitry or potentially rocket control surfaces.

Acknowledgements

There are several people without whom this research would not have been possible. To these, I extend my sincere gratitude.

The thoughtful guidance of my research advisor, Kris Pister, provided direction for this project from its inception. His boundless vision and enthusiasm embody the true spirit of engineering research and innovation.

Al Pisano graciously gave his time and insight as part of my committee. Although I knew only his legacy for most of my time here, he has been a great proponent of this research.

This work was initiated by Carole Rossi of *Laboratoire d'analyse et d'architecture des systemes*. I cannot forget her introduction to the world of propellant combustion behind Cory Hall.

Much of the early work on this project was done in collaboration with Lance Doherty. He also provided valuable feedback as a proofreader for this report. His wit and *anschauung* have been a pleasure.

Paul Chang and Brandon Brown put many hours into thrust testing. I am grateful for their efforts and for putting up with me.

Thanks to Lilac "Process Queen" Muller for introducing me to the microlab and helping with process design and fabrication.

Veljko Milanović has been a driving influence in the completion of this project. His help with fabrication and testing was invaluable, but more than that, his patience and willingness to impart wisdom, knowledge and motivational energy have been a testimony to his selfless work ethic and mentorship.

Funding of this project has provided by the Defense Advance Research Projects Agency and the National Science foundation, to which I am grateful for their generous support.

To all the students of 471 Cory, I am grateful for their always insightful comments and camaraderie. It's been fun!

Thanks also to my Veritas friends and small groups. Through your support, encouragement and fellowship, I have experienced God's faithfulness.

Mel, thanks for keeping me sane by relaxing with me for those short, yet precious moments.

To my family who has supported me always, I'm glad you have been there to commiserate with me through the struggles and rejoice in the triumphs. I'm thankful for the examples of honesty, integrity and love of God you set for me.

Table of Contents

1. Introduction

The goal of this research is to develop a millimeter-scale rocket capable of one-time flight with integrated thermal power converters for generating electrical power during propellant combustion. Although rockets have been made on a larger scale for hundreds of years, several challenges stem from scaling rocket geometries to the millimeter scale. Among these challenges are the fabrication and integration of micro components, inherent propellant flammability limits, and increased thermal losses due to surface area-to-volume scaling.

Advances in micromachining technology make possible the patterning and etching of submicron geometries in a variety of materials. In the microrocket system, micromachining techniques are used to fabricate the rocket nozzle with integrated ignition and thermal power conversion devices. Even though micromachining techniques as presented enable microrocket fabrication, the fundamental physics of the rocket system and scaling implications cannot be ignored and will be discussed throughout.

The microrocket system discussed herein integrates rocket propellant, a ceramic combustion chamber, silicon micromachined nozzle, polysilicon igniter, and thermal power converters for generating electrical energy during rocket flight. Theory, fabrication of components, testing, simulation, and integration aspects will be discussed. By no means is microrocket performance optimized in this body of research. Rather, the successes and failures of a comprehensive microrocket system are presented, inviting further investigation of the limits and potentials of microrocket fabrication, flight, and integration.

1.1 Application: Smart Dust Delivery

Advances in the fields of digital circuitry, wireless communications and microelectromechanical systems (MEMS) converge in the development of tiny, low-power, low-cost, autonomous sensor nodes known as Smart Dust, an ongoing research project at the Berkeley Sensor and Actuator Center [1]. Each Smart Dust mote is designed with its own suite of MEMS sensors, wireless communications, computing hardware, and a power supply, all within a few cubic millimeters (Figure 1). Thus far, advances in line-of-sight optical communication using corner cube reflectors (CCR) [2] as passive transmitters and large DC deflection 2-DOF micromirros for beam steering have been reported [3]. Additionally, preliminary platforms designed to test incoming optical signal decoding, generate simulated sensor data with a pseudorandom number generator and drive a CCR have been designed and fabricated in a 0.25 μm CMOS process [4]. Equipped with the latest MEMS sensor technologies, networks of hundreds of Smart Dust nodes could be deployed for monitoring device characteristics, chemical concentrations, or other environmental data. By deploying Smart Dust over large areas, such as around a planet, with some minimum spacing between motes, a communication network can be formed and data from any mote in the

network could eventually reach a single base station. With these possibilities, one question that remains to be addressed is: how will Smart Dust be deployed?

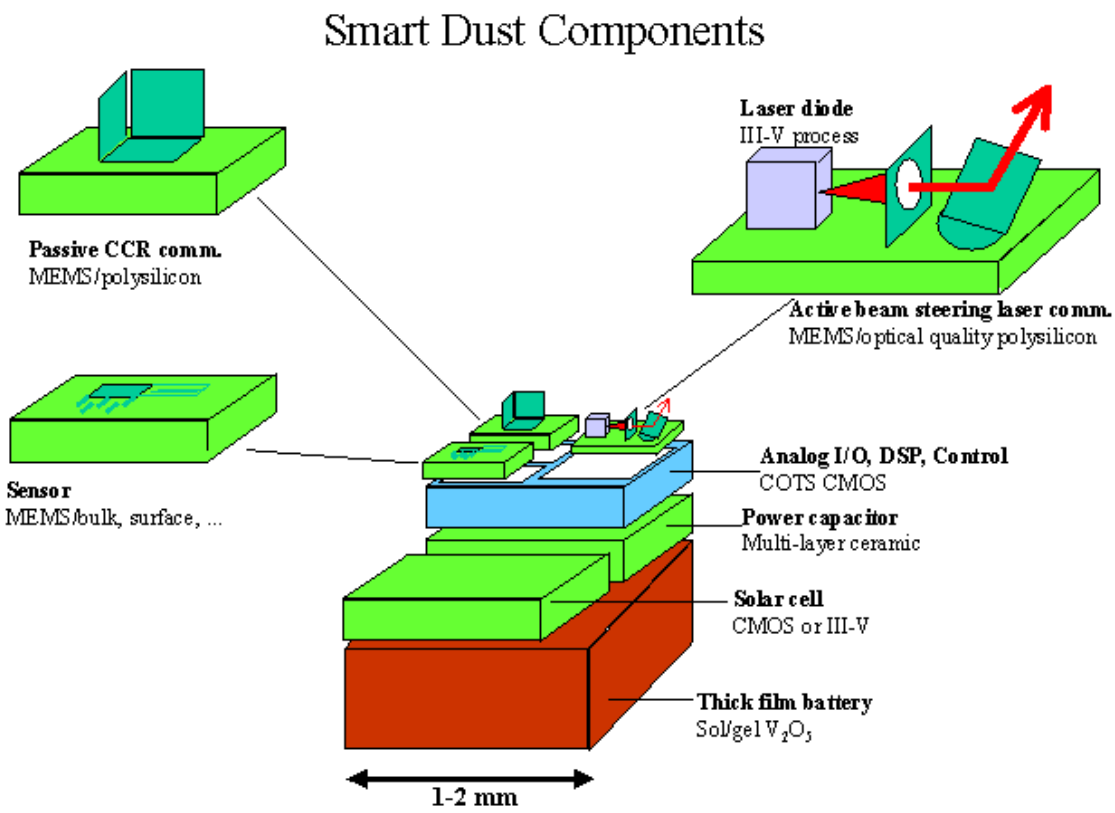

Figure 1. Diagram of Smart Dust components.

Potential deployment options include dropping or scattering several Smart Dust motes by hand or from micro air vehicles (MAV). This type of deployment will lead to dense mote distributions in some areas and very sparse distribution in others. By deploying each mote from a base station or MAV with a single-use microrocket, the Smart Dust distribution area could be expanded by shooting motes in different directions. Microrockets could also be used for Smart Dust deployment in situations where distribution by humans may be hazardous, such as in space as illustrated in Figure 2.

1.2 Challenges in Rocket Miniaturization

Miniaturizing a rocket system presents challenges requiring careful consideration of propellant selection, material selection, rocket geometry, and integrated device characteristics. The major scaling-related issues considered in this research are:

- Rocket fuel selection - A high energy density propellant that combusts though small cross sections is required.

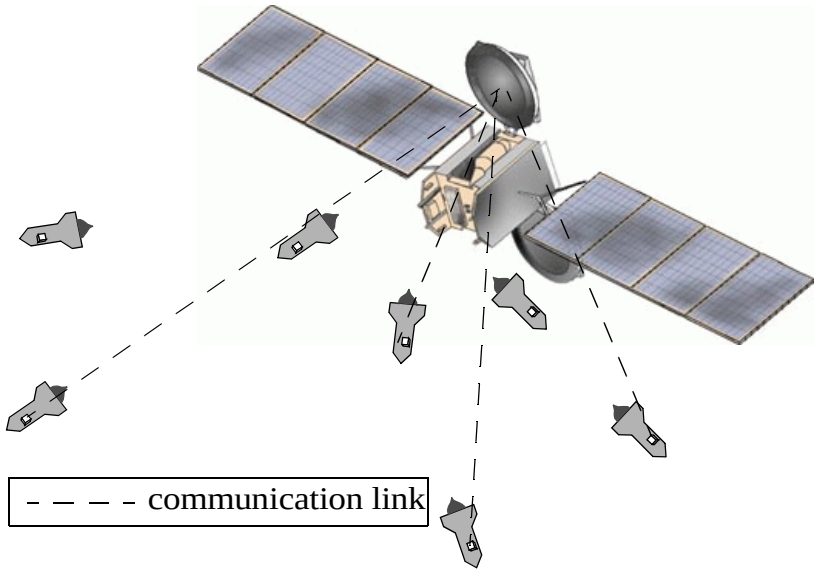

Figure 2. Microrockets with Smart Dust payloads deploying and maintaining periodic communication with satellite.
(satellite image courtesy of TheTech museum of innovation)

• Combustion - Since chemical reaction rates do not scale with size, combustion must be completed during the propellant's residence time inside the combustion chamber.

• Ignition - Adequate energy must be supplied to the propellant by a microfabricated structure to ignite the propellant.

• Propellant housing - Combustion chambers must provide thermal insulation to burning propellant and sustain high temperatures and internal pressures.

• Assembly and Fabrication - The rocket assembly volume and weight should be minimized for flight capability. The use of microfabrication techniques is desirable for batch fabrication, low cost, and integration with micromachined components.

• Power conversion - Efficient thermal power converters are necessary to generate useful levels of electrical power during microrocket flight.

1.3 Previous Micropropulsion Work

Most previous work toward the development of micropropulsion systems has been for the purpose of low-thrust generation for nanosatellite and microsatellite station-keeping and maneuvering applications. Janson *et al* [5],[6] discuss microfabricated cold gas thrusters, digital thruster arrays, resistojets, and field ion engines. These thrust-producing devices have been fabricated through various micromachining processes with thrust up to 1 mN for cold gas thrusters, and impulses in the 0.09 mN-s range for the digital thrusters. The digital thrusters fabricated in this

study used resistive heaters to ignite a solid explosive which exited the combustion cavity primarily unburned. Bayt [7] reports cold gas expansion microthrusters fabricated in a process allowing arbitrary nozzle geometry within two dimensions. Bayt's gas expansion thrusters produced thrust in the 0-12 mN range for chamber pressures up to 100 psia. Other solid propellant microthrusters were developed by Rossi *et al* [8], with thrusts of up to 1 g (equivalent to 9.8 mN). While effectively producing the thrust levels required for some microsatellite and nanosatellite positioning applications, none of these systems have been designed specifically for flight, and most require some sort of sustained power input or gas hookup during operation.

1.4 Overview

This section presented research goals, described Smart Dust and the application of microrockets for Smart Dust delivery, stated the major challenges involved in miniaturizing a rocket system, and gave a brief overview of previous work on micropropulsion systems.

Section 2 addresses the choice of propellant for the rocket and parameters influencing combustion as it relates to microrocket performance.

Section 3 discusses the theory governing thrust generation, nozzle geometry and overall system efficiency.

Section 4 introduces the design and fabrication of the microrocket assembly.

Section 5 reports measured performance of microrocket components.

Section 6 gives an overview of thermal power conversion theory and presents simulation and performance of fabricated thermopile devices.

Section 7 summarizes results and presents recommendations for improvements and advancements of the system.

2. Propellant

Despite demonstrated rocket propulsion by methods including nuclear thermal rockets, ion propulsion, and hall effect thrusters, chemical rocket engines remain the most commonly used type [9]. Chemical reactants are second only to nuclear fuels in terms of energy density, which for kerosene is on the order of 3.5×10^7 J/L [10]. Chemical propellants have also been widely researched and used reliably in applications ranging from booster rockets for the space shuttle to numerous hobby rockets. Due to proven reliability and wide availability, only chemical propellants were considered for this research.

2.1 Types of Rocket Fuel

The characteristics of different types of chemical rocket propellants were investigated to choose the most appropriate fuel for a microrocket. Chemical propellants are usually either solid or liquid (Figure 3). Solid propellants are easy to use without special operating and handling

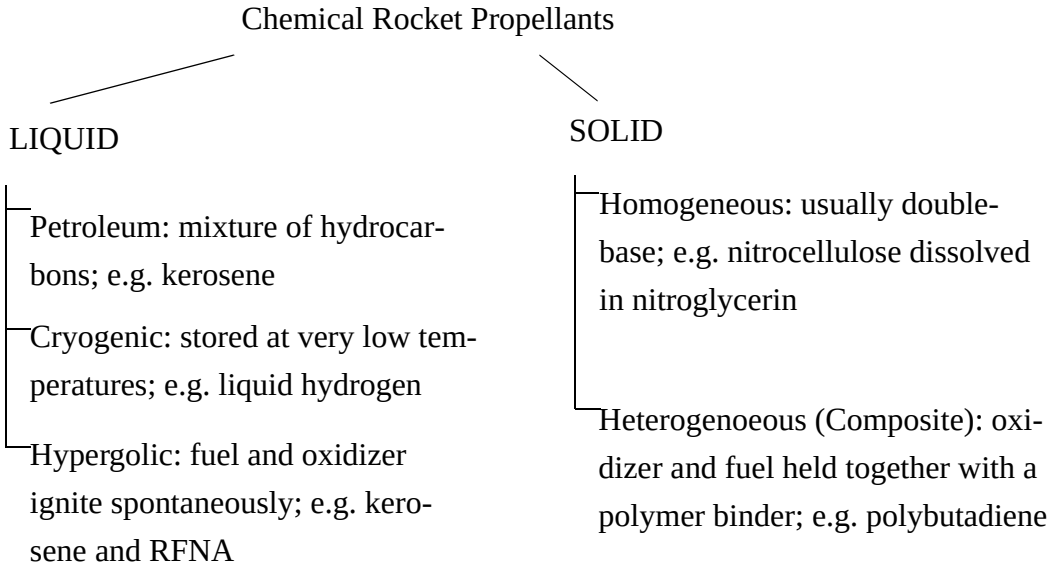

Figure 3. Types of chemical rocket propellants

equipment and the fuel and oxidizer can be stored mixed at room temperature. Liquid propellants are composed of liquid fuels and oxidizers that are stored separately and mixed at the time of combustion. They require systems for storage and usage, including pumps, valves and sometimes cryogenic tanks. For some applications, however, the complexity of handling liquid propellants is warranted because they often have higher specific impulses than solid propellants, and combustion can be readily throttled or stopped altogether.

The metric for evaluating propellant performance is the specific impulse (I_{sp}), which describes the total force integrated over burning time per unit weight of the propellant. For constant thrust and propellant flow, I_{sp} is given by:

$$I_{sp} = \frac{Ft}{mg}$$

where Ft is the total impulse (N-s) in which F is thrust (N), t is time (s), m is propellant mass (kg), and g is the gravitational constant (ms^{-2}). The specific impulses of several common chemical propellants are listed in Table 1.

Propellant[a]	Type	I_{sp} [s][b]
Hydrogen/Fluorine	Liquid	410
Hydrogen/Oxygen	Liquid	390
75% Ethyl Alcohol/Oxygen	Liquid	279
AP-based with Al	Solid	260-265
DB	Solid	220-230
Polymer/AN	Solid	180-190

Table 1. Specific Impulse of Various Chemical Propellants (adapted from Sutton)[11]

a. AP: Ammonium Perchlorate, DB: Double Base, AN: Ammonium nitrate
b. For 1000psi combustion chamber expanding to 1 atm (14.7 psi) - implies optimal nozzle expansion

2.2 Advantages to Solid, Heterogeneous Chemical Propellant

To achieve the smallest overall structure while preserving design simplicity and relatively high specific impulse, a solid, composite fuel with ammonium perchlorate oxidizer (AP) was chosen. The composite fuel is based on a standard propellant recipe provided by [12], and contains 74% AP, with 14% hydroxyl-terminated polybutadiene (HTPB) fuel binder, along with the other ingredients listed in Table 1. Solid propellants with AP oxidizer generally have energy densities of approximately 5 kJg^{-1} and specific impulses up to 265 s (for 1000 psi chamber pressure expanding to 1 atm).

Ingredient	% by mass	function
Ammonium Perchlorate	74	oxidizer
R45-M resin (HTPB)	14	binder/fuel
2 - Ethylhexyl Acrylate (EHA)	6.5	plasticizer
Isophorone Diisocyanate (IPDI)	3.5	curing agent
Fe_2O_3	1.25	combustion catalyst
HX-878 (Tepanol)	0.75	bonding agent

Table 2. Propellant Ingredients [12]

2.3 Composite Propellant Ignition and Combustion

Ignition occurs when sufficient energy is introduced to the propellent through exposure to a hot surface, radiant energy source, hot inert gas, pilot flame, explosive charge, or electrical spark. Leading up to ignition, external heating of the propellant creates a temperature rise that initiates chemical reactions at the propellant surface. These chemical reactions are exothermic, further increasing the temperature and chamber pressure until ignition occurs and steady-state combustion ensues.

Factors influencing ignition include igniter temperature, the duration that the propellant is exposed to the igniter, and the area of fuel surface exposed to the ignition surface. Strong, or high-power sources, that reach temperatures near the propellant flame temperature tend to ignite propellant quickly, while weak sources require a longer exposure time [13].

The following discussion is motivated by research involving ignition and combustion of AP-based propellants, as compiled by Kishore and Gayathri [14]. Ignition theories of AP-based propellants suggest that while the influx of heat from an outside source catalyzes surface reactions of the propellant, it is the exothermic reactions taking place at or near the surface of the propellant that allow conditions suitable for combustion to be reached. From this information, ignition can be thought of in two phases. First, the initiation by an outside heating source, and second, exothermic chemical reactions on the propellant surface which lead to ignition. When taking place in a combustion chamber, the pressure rises only slightly as a result of the ignitor heating, plateaus for a short time, then rises more during the second phase, and reaches the design chamber pressure after full-fledge combustion begins.

AP is stable at room temperature, which makes safe propellant storage easy. Around 420 K, decomposition begins, and between 520-620 K, it goes to completion, corresponding with the propellant ignition temperature. Additionally, above 700 torr (1 atm = 760 torr), AP decomposes completely, as depicted in Figure 4.

At ambient pressure, oxidizer decomposition is the controlling reaction. AP also decomposes slower than the fuel binder at temperatures less than 650 K. Since the surface temperature of the propellant is expected to be below 650 K at ignition, AP decomposition is assumed to be the limiting reaction during ignition. As might be expected, it is also reported that AP contributes significantly to ignition in low oxygen atmospheres.

During combustion, decomposition of AP (NH_4ClO_4) and the fuel binder, HTPB, into gaseous products takes place at the propellant surface, with decomposition occurring as shown in Figure 4 [14]. The decomposed products of the fuel and oxidizer must mix in order for the combustion reaction to take place. Diffusional mixing is the critical step in this process which results in the combustion reaction several microns away from the fuel surface. Low pressure and small

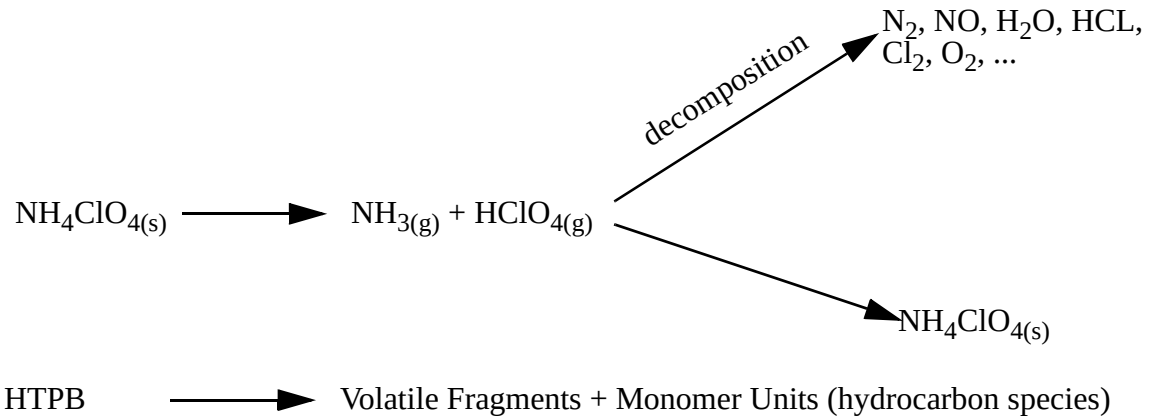

Figure 4. Decomposition of AP and HTPB fuel binder, after [14].

AP particle size result in more complete mixing before combustion. Some research suggests that a melt layer exists on AP particle surfaces during propellant burning, however, at atmospheric pressure, the burning surface is dry. SEM photographs of polybutadiene propellants showed that protrusions of AP particles exist at the burning surface under some conditions; however, decreased particle size, lower AP loading, or increased pressure leads to a plateau effect, where the flat surface of the binder extends above AP particle positions. Extreme cases of the plateau effect are to be avoided since melted binder can flow over AP crystals, thus extinguishing the flame. These results imply that the respective decomposition rates of AP particles and binder are dependant on AP particle characteristics and environmental conditions. A general illustration of an AP-based propellant mixture is shown in Figure 5.

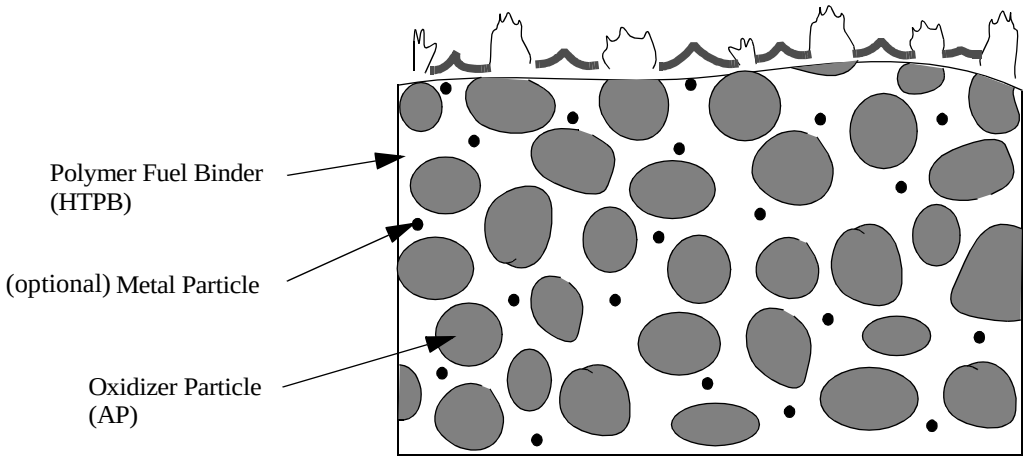

Figure 5. Diagram of heterogeneous (composite) solid propellant. Oxidizer particles are suspended in fuel binder, and each produces a different flame at the propellant surface.

Despite the disadvantage of decreased AP particle size contributing to the plateau effect, the use of fine AP particles can be used as a burn rate enhancer [11]. Because the burn rate will be slowed in a microscale system due to high thermal losses, an increased burn rate by means of AP particle size variation becomes desirable. Therefore, to avoid extinction brought on by fine AP particles while maintaining an acceptable burn rate and a well-mixed flame, a blend of coarse and fine AP particles (usually in the range of 5-600 μm) can be used. Additives such as aluminum (Al) particles may also be used increase the burn rate and will be discussed further in 2.4.

2.4 Propellant Testing

The propellant mixture in Table 2 was varied by changing the size of the AP particles and by adding Al particles. Mixtures with varying AP size were burned through small channels and observed to determine which mixture burns most readily without extinction. Propellant mixtures with added Al of varying particle size were burned inside ceramic combustion chambers and compared to propellant without Al to determine usability in microrockets. Video records indicate whether complete combustion occurs inside the chamber.

AP Particle Size

Variations in AP particle size were observed to have an impact on the propellant's capacity to burn through small cross sectional areas. The propellant mixture containing AP particles which were ground smaller than their original 200 μm diameter was found to ignite and sustain combustion through small cross sections more readily than the mixture containing only 200 μm particles. This supports the information presented above from [14]; if the oxidizer particles are large and spaced far apart, the gasified oxidizer and fuel may not mix adequately in a small chamber to maintain the exothermic combustion process.

Adding Aluminum

Adding Al particles to composite propellants increases the burn rate, flame temperature, and I_{sp} of the fuel [12]. Al was added to the HTPB/AP composite fuel and ignited by a thin wire filament inside a a 3x4x1.5 mm ceramic combustion chamber. The added Al did result in an increase in burn rate; however, Al particles were visibly combusting after exiting the chamber, and were found to clog sub-millimeter nozzles. This agrees with Sigman *et al* [15], that during combustion Al particles tend to agglomerate at the burning surface and exit the combustion chamber without fully burning. Combustion flames for HTPB/AP and HTPB/AP/Al in 3x4x1.5 mm ceramic combustion chambers are shown in Figure 6 a and b, respectively. The inability of Al to combust inside a millimeter-scale chamber is an indication of how scaling can affect rocket performance. Specifically, this result emphasizes that the residence time of combustion species in

the combustion chamber must be longer than chemical combustion reaction rates. HTBP/AP fuel mixture without Al was used for all subsequent testing.

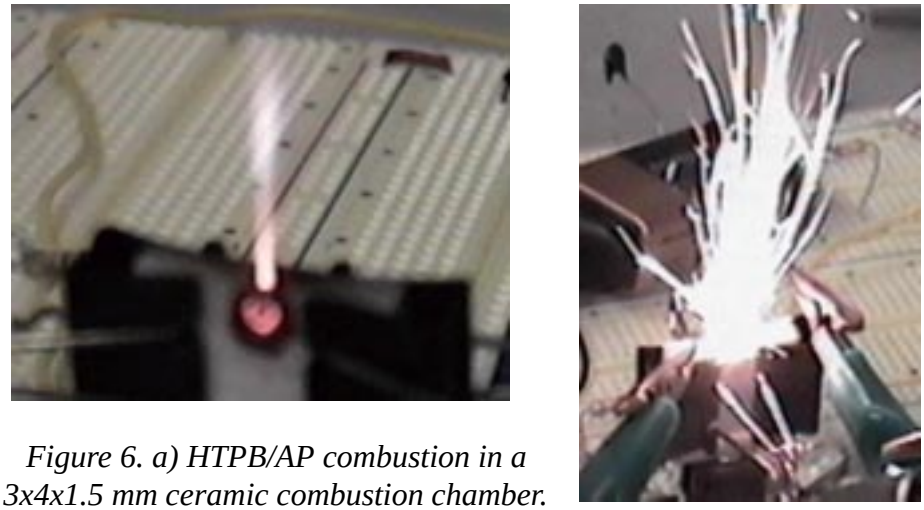

Figure 6. a) HTPB/AP combustion in a 3x4x1.5 mm ceramic combustion chamber. b) HTPB/AP/Al combustion in same chamber. Particulate ejection indicates incomplete combustion during residence time in chamber.

3. Propulsion

As a general definition, propulsion is the act of changing the motion of a body. The term *rocket propulsion* describes a broad range of propulsive devices that produce thrust by ejecting stored matter or propellant [11]. Rockets can use chemical, solar, or nuclear energy for propulsion and may be designed for one of a variety of functions, such as station keeping, booster stages, or attitude control. This section will focus on how thrust is generated in rocket propulsion systems.

3.1 Thrust

The principal describing rocket thrust is Newton's Third Law of motion, which states that every action has an equal and opposite reaction. Since momentum is conserved in the rocket shown in Figure 7, the change in momentum of the rocket can be equated to the change in momentum of the exhaust:

$$\left(\frac{\Delta M}{\Delta t}\right)v + M\left(\frac{\Delta v}{\Delta t}\right) = \frac{\Delta M}{\Delta t}(v - u)$$

As Δt approaches zero, this becomes:

$$M\frac{dv}{dt} = -u\frac{dM}{dt}$$

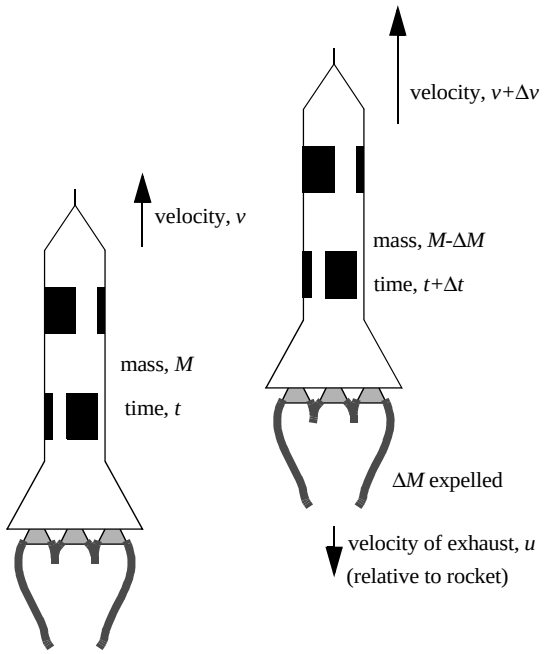

Figure 7. Illustration of rocket motion from time t to time t+Δt

Thrust will always be positive because *dM* will always have a negative value since the rocket is losing mass while operating. This equation is useful only in the ideal case where external forces, such as gravity and drag forces, are neglected. Including external forces (F_{ext}) gives:

$$M\frac{dv}{dt} = F_{ext} - u\frac{dM}{dt}$$

This equation makes it clear that a large exhaust gas velocity and a rapid decrease in propellant mass result in high thrust values.

The structure of a rocket allows it to convert combustion energy into thrust. Some parts are common to almost all conventional composite rockets, including a combustion chamber, a propellant grain, an igniter, and a nozzle. The design of these parts, along with surrounding conditions determine the amount of thrust generated and the efficiency with which thrust can be produced.

An examination of the pressure distribution inside and outside of the rocket reveals how the combustion chamber and nozzle structure enables the conversion of hot combustion gases into thrust. Various gases and heat are the products of the solid propellant combustion reaction. Thrust is produced when these hot gases are accelerated as they pass through the narrow throat area of the nozzle and subsequently ejected from the rocket. As a result, the pressure of the gas decreases as it leaves the high-pressure combustion chamber. In Figure 8, the pressure distribu-

tion along the sides of the combustion chamber is balanced; however, the pressure exerted at the top of the chamber is unbalanced, thereby resulting in a an upward force (F) on the rocket.

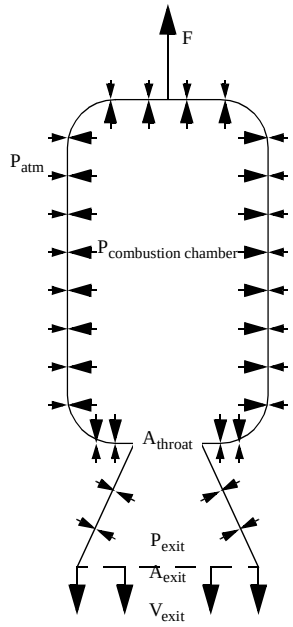

Figure 8. Pressure distribution around a rocket

3.2 Nozzle

Most basic conventional nozzle theory is reliant upon several assumptions, many of which cease to be applicable as the nozzle size decreases. These assumptions are stated in the development of nozzle theory in [11]. Specific assumptions which might be significantly unfit as rocket dimensions decrease include the following: flow is adiabatic (no heat transfer to walls) and steady, there are no friction or boundary layer effects, and chemical equilibrium occurs in the combustion chamber such that no further chemical composition changes occur outside of the nozzle. It remains, however, that optimum nozzle expansion is achieved when the pressure at the nozzle exit is the same as the atmospheric pressure. A nozzle is underexpanded when the pressure at the nozzle exit is greater than atmospheric pressure. By contrast, an overexpanding nozzle has too large of an exit area resulting in gas expansion to pressures lower than atmospheric pressure. Figure 9 depicts flow in an optimally expanded nozzle, an underexpanded nozzle, and an overexpanded nozzle.

The divergence angle of a nozzle refers to the angle of the nozzle cone for a conical nozzle. Small divergence angles result in high I_{sp} since almost all of the momentum is axial. The disadvantage of very small divergence angles is that they must be very long to expand the exhaust gas to its optimal pressure. Conventionally, optimum divergence cone half angles are between 12^{o} and 18^{o}.

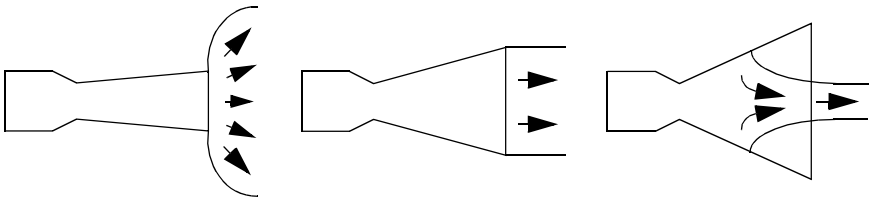

Figure 9. Depiction of exhaust flows in underexpanded, optimal and overexpanded nozzles.

A closely-related nozzle parameter to the divergence angle is the nozzle area ratio, which is the area at the nozzle exit divided by the throat area. The dependence of thrust on nozzle area ratio is strongly dependent on the specific heat ratio of the exhaust gas, which is generally in the range of 1.0-1.6 for gases exhausted during propellant combustion. Given this range of specific heat ratios, an area ratio of unity, indicating a non-diverging nozzle, can decrease thrust generation by over 60% of maximum thrust [11].

Early gas expansion micronozzles fabricated in PMMA using only X-Y laser micropositioning (all angles are 90^{o}) were reported by Janson and Helavijian [6] as having I_{sp} values up to 83% of ideal I_{sp} values, suggesting that significant thrust can be generated when using crude microscale nozzle geometries. A more detailed study of 2-D micronozzle performance was performed by Bayt [7]. Numerical modeling and testing of fabricated nozzles were used to determine the dependence of I_{sp} and thrust efficiencies on Reynolds numbers from 0 to 4000 and area exit ratios from 5.4 to 16.9. Findings include that I_{sp} and thrust efficiencies, defined by performance versus quasi 1-D predictions, increase significantly with increasing *Re*, and begin to plateau around an *Re* of 2000. Also, I_{sp} efficiency increased to nearly 100% for increasing area ratios at higher *Re*. For values of *Re* lower than about 500, simulated efficiencies of small area ratio nozzles were slightly more efficient than for larger area ratio nozzles, suggesting that the boundary layer plays a bigger role as *Re* decreases. This confirms that in scaling down nozzles, the boundary layer cannot be neglected. In fact, the effective area ratio is governed in large part by the presence of the boundary layer. With this in mind, the width and location of the boundary layer may be as important to consider as the physical nozzle geometry for optimizing microscale nozzles.

3.3 Efficiency

The ultimate *quaesitum* of microrocket design is to efficiently convert chemical energy into kinetic energy in order to produce axial thrust. Looking at the energy balance of a large rocket system can help to emphasize the effects of scaling a rocket down to millimeters. Table 3

summarizes the typical sources of energy loss for a chemical rocket given in [11]. The major

Energy Loss Mechanism	% of Total Energy Lost
Combustion loss (poor mixing/incomplete burning)	1
Heat loss to walls	2
Unavailable thermal energy of exhaust jet	27-57
Residual kinetic energy of exhaust gas	0-50

Table 3. Energy loss mechanisms in a typical chemical rocket

sources of energy losses in a traditional chemical rocket are due to unharnessed thermal energy and residual kinetic energy, while combustion losses and heat loss are comparatively negligible. By decreasing the combustion chamber size and thereby increasing the surface area to volume ratio of the rocket, it is expected that combustion losses and heat losses will increase significantly. Combustion losses will increase since the diminished combustion chamber volume will decrease combustion reactant residence time before exiting the rocket, contributing to incomplete burning. Heat loss to the combustion chamber walls is expected to increase since the wall surface area versus the volume of propellant increases linearly with scale. Also, heat transfer per unit area by means of conduction and convection is inversely proportional to the characteristic length scale of the system, as given by:

$$\frac{q_k}{A} = \frac{k}{L}(\Delta T) \qquad \text{Conduction}$$

$$\frac{q_c}{A} = Nu\frac{k}{L}(\Delta T) \qquad \text{Convection}$$

where, q_k and q_c are heat conductive and convective heat flow rates (W), respectively, A is area (m^2), k is thermal conductivity ($Wm^{-1}K^{-1}$) of the material or fluid, Nu is the non dimensional Nusselt number that describes the ratio of the temperature gradient in the fluid immediately contacting the surface to a reference temperature gradient, L is length (m), and ΔT is the temperature differential (K). This means that the heat flow per unit area increases as rocket size decreases. Heat is also transferred through radiation, but heat transfer per unit area for radiation does not scale with length.

Apart from thrust generation, an objective of the presented system is to recapture a portion of the thermal energy lost through the implementation of thermopiles for thermal power conversion. Although this energy will not necessarily aid in propulsion, it could function as a power supply for on-board sensors or rocket control surfaces. Unfortunately, thermal conversion effi-

ciencies generally reach only about 10% when optimized; however, the large heat dissipation of the rocket may make useful power levels available despite the low conversion efficiency. The end result is that the microrocket system efficiency will improve since less energy is lost to the surroundings.

4. Design & Fabrication

The microrocket assembly has two basic components: a combustion chamber and a nozzle. The combustion chamber houses the solid propellant, while the nozzle is a constriction at the combustion chamber exit that allows hot combustion gases to accelerate as they exit the rocket, thereby increasing thrust. Igniters and power-converting thermopiles are fabricated on the same silicon substrate that the nozzle is etched into, and will be discussed in more detail in subsequent sections.

4.1 Combustion Chamber

Investigations of combustion chambers made of various materials were conducted. 2-D combustion chambers were fabricated in copper, aluminum, brass, carbon steel, and stainless steel by wire electrical discharge machining (EDM), and in ceramic by conventional machining. Similar chambers were also fabricated in silicon using deep reactive ion etch (DRIE). In this process, wafers of silicon combustion chambers, as shown in Figure 10, were fabricated with a single photolithography step followed by DRIE through the wafer. Each 2-D chamber had a cross section similar to the design shown in Figure 10.

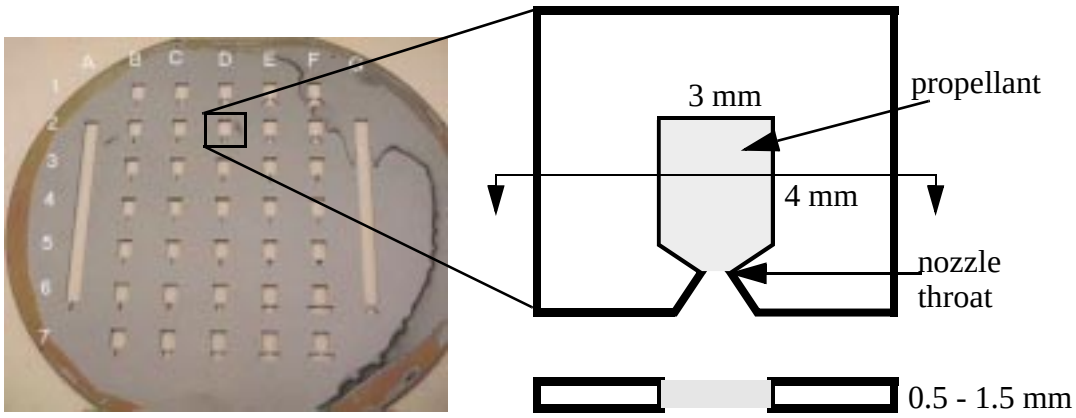

Figure 10. Silicon wafer with DRIE combustion chambers and nozzles, and detail of chamber design.

In preliminary tests, the 2-D combustion chambers made of various materials were filled with HTPB/AP composite fuel and sealed by epoxying glass plates to the chambers. Ignition was achieved by heating a thin wire filament in contact with the fuel at the nozzle opening. Testing

showed that at room temperature, combustion is difficult to sustain through the entire 4 mm length of a 2-D combustion chamber, with the only repeatable sustained burn occurring in the ceramic combustion chambers. This result suggested the need to choose a combustion chamber material with low thermal conductivity, since heat loss through the chamber walls removed enough energy from the burning fuel to quench combustion in the silicon and metal chambers. Additionally, the 1.5 mm glass covers to the chambers were found to crack during combustion due to the high pressure and temperature generated in the combustion chamber, indicating the need for stronger chamber walls.

An alumina ceramic cylindrical combustion chamber design addresses the needs of thermal insulation and strength. Alumina ceramic has a thermal conductivity of 30 $Wm^{-1}K^{-1}$, five times lower than the thermal conductivity of silicon. Additionally, the cylindrical shape reduces the surface area by 13% compared to a 1.5 mm thick rectangular chamber having the same length and volume. This also serves to reduce the overall volume occupied by the chamber since less wall surface is required, thus reducing the mass of the rocket. The cylindrical chamber also has a structural advantage over the flat, rectangular chamber since it is able to resist bending and cracking, which the walls of the rectangular chamber are prone to do. The main disadvantage to alumina ceramic cylinders is that they are not microfabricated, and must be machined separately. A more exhaustive investigation of materials and chamber geometries might further minimize combustion chamber mass, volume and thermal conductivity while maintaining strength.

4.2 Nozzle with Integrated Igniter & Thermopiles

The nozzle portion of the rocket was fabricated using silicon micromachining techniques, which allow the integration of an igniter and thermopile for power conversion with each rocket nozzle. Figure 11 is a CAD rendering of the rocket assembly including the ceramic combustion chamber with epoxy cap and the silicon nozzle die. On the nozzle die, igniters and thermopiles were surface micromachined out of polysilicon and aluminum conductive layers, with low stress nitride (LSN) insulating layers, as shown in steps 1 through 5 of Figure 12. In step 6, surface micromachining is followed by a backside deep reactive ion etch (DRIE) through the 300 μm-thick silicon wafer. The backside etch creates the nozzle opening and thermal isolation cavities. When these cavities are created, the igniter and thermopiles become suspended on LSN membranes.

The patented Bosch process as described in [16] was used in the backside DRIE to form the nozzle and thermal isolation holes. This process etches deep, high aspect ratio trenches in silicon. As a result, nozzles with negligible expansion angles were formed. An alternative method of micronozzle fabrication in silicon is reported by Janson and Helvajian in [5], which describes an anisotropic KOH etch of silicon. KOH etches silicon selectively along the <100> planes,

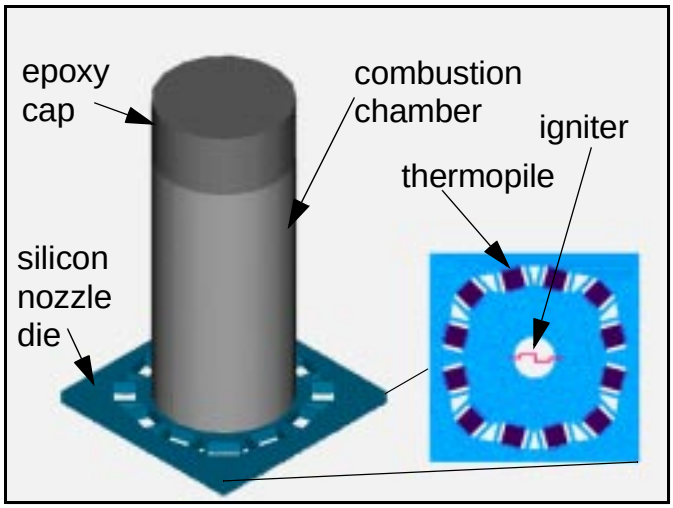

Figure 11. CAD rendering of rocket assembly and nozzle die.

while almost stopping on the <111> planes, resulting in a 35^{o} angle between the nozzle edge and the center line.

In general, a nozzle is considered optimal when the pressure of the gas as it exits the nozzle is the same as the ambient pressure, as discussed in 3.2. In comparison to most optimized rocket nozzles, the DRIE nozzles are underexpanded while the KOH-etched nozzles are overexpanded. In both cases, nozzle efficiency is not optimized; however, the underexpanded case is generally preferable to the overexpanded case since the drag and non-axial component of the gas velocity are smaller. As reported in [16], varied trench depths and widths have been achieved through altering DRIE process parameters. Therefore, by closely controlling the etch process, it is likely that arbitrary nozzle geometries could be formed.

4.3 Assembly

Rocket systems are assembled by packing uncured propellant into the cylindrical ceramic combustion chambers, allowing the propellant to cure to a firm, rubber-like grain. Propellant loses about 1% of it's mass while curing and increases slightly in volume. Curing is followed by bonding the propellant-filled combustion chamber and the nozzle die together with high-temperature epoxy. The open end of the combustion chamber is also sealed with epoxy. Figure 13 shows the assembled rocket, and Figure 14 shows the fabricated nozzle die.

1. Deposit oxide followed by 1 μm low stress nitride (LSN).

2. Deposit and pattern 0.3μm p-doped poly followed by 0.6μm LSN.

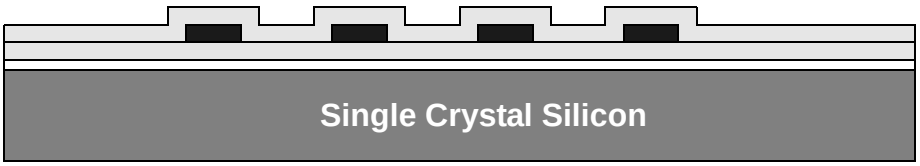

3. Deposit and pattern 0.6μm n-doped poly followed by 0.6μm LSN.

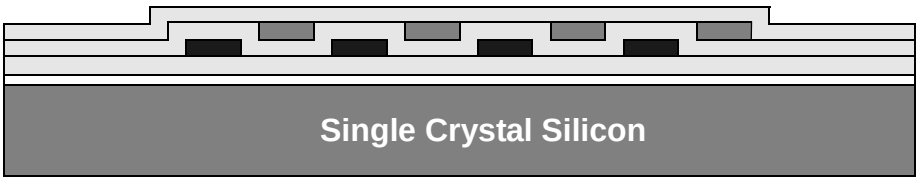

4. Etch nitride to form contacts to poly and opens.

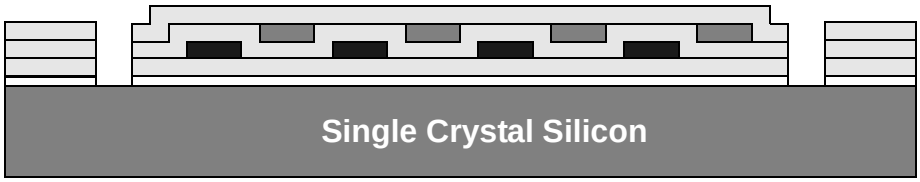

5. Deposit and pattern 1 μm aluminum.

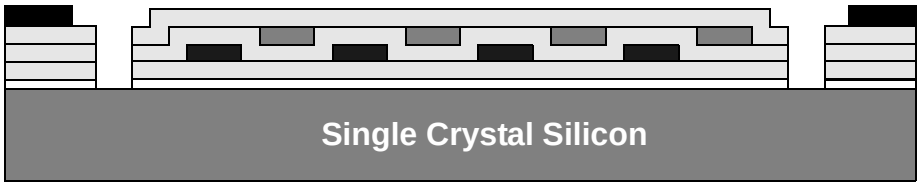

6. Backside DRIE to suspend thermopile and nitride membrane.

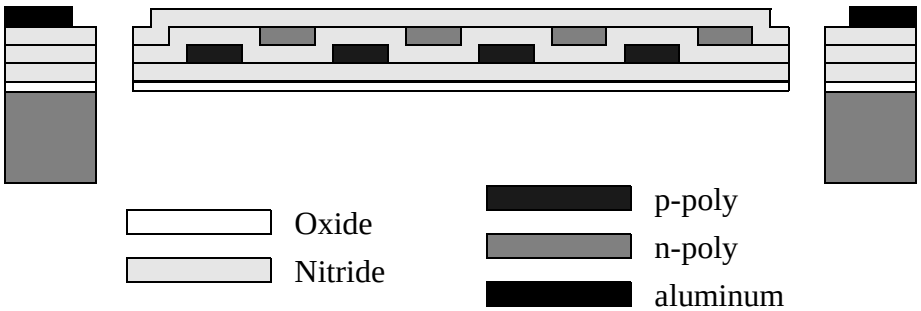

Figure 12. Fabrication process flow showing thermopile fabrication. Igniters and nozzles are also made in this same process.

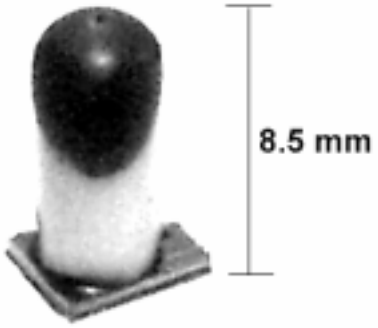

Figure 13. Assembled microrocket with ceramic combustion chamber epoxied to silicon nozzle die

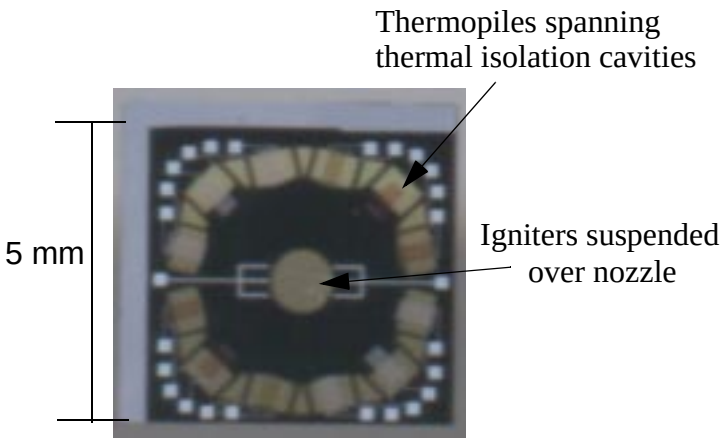

Figure 14. Fabricated silicon nozzle die showing igniters and thermopiles suspended on LSN membranes

5. Rocket Performance

Ignition and thrust generation are two of the most important aspects of any rocket. Characteristics of functional igniters are addressed in this section, as well as rocket thrust generation. In order to promote continued parallel development of the microrocket components, thrust generation through combustion chamber and nozzle geometry, igniter performance, and thermopile effectiveness (to be addressed in later sections) were tested independently using simplified strategies rather than as a fully integrated unit. The results obtained, however, reflect the expected performance of the amalgamated system.

5.1 Ignition

High-voltage spark generators, match and torch flames, and electrically heated wires were all found to ignite HTPB/AP. Although each of these methods initiates ignition, a successful microrocket ignition system must not only reliably ignite the chosen HTPB/AP propellant, but it must also be easily integrated with the rest of the rocket components. Of these methods, the widely-used concept of electrically-heated thin wire ignition was extended into the microfabrication domain, from which the use of polysilicon resistive heaters as igniters was pursued.

Igniter Characteristics

An array of polysilicon heaters was fabricated using the process described in 4.2. The array consisted of straight and meandering heater designs with polysilicon widths ranging from 8 μm to 80 μm, lengths varying from 450 μm to 1050 μm, and a polysilicon thickness of 0.3 μm with sheet resistance of 25 Ω/square. Heaters were tested for their ability to ignite HTPB/AP propellant by placing a small slab of propellant directly on top of the suspended heaters. Ignition was achieved by three meandering heater designs, and no straight designs. The lengths, widths and resistances of successful igniters are given in Table 4. Figure 15 is a scanning electron micrograph of a suspended polysilicon heater, with an inset of its heating profile as measured by a temperature-scanning microscope. Thermal isolation through suspending the heater on a membrane localizes high temperature regions on the heater, with little heat dissipation to the surroundings areas.

	Length [μm]	**Width [μm]**	**Resistance [kΩ]**
heater 1	1050	16	2.65
heater 2	1050	8	5.95
heater 3	850	40	0.80

Table 4. Polysilicon Igniter Characteristics

In order to increase the reliability and area over which heat is generated by the polysilicon igniters, three polysilicon heaters of heater 1 type (from Table 4) were connected in parallel and suspended over the 1 mm-diameter nozzle opening in an LSN membrane. This design was robust in the sense that ignition was still achievable even when there was damage to one or two of the suspended heaters, and in some trials, heaters were still functional after fuel burned directly on top of them.

Both n-poly and p-poly igniters were fabricated using the three parallel igniter design, with a p-poly thickness of 0.6 μm and an n-poly thickness of 0.3 μm. Sheet resistances of p-poly

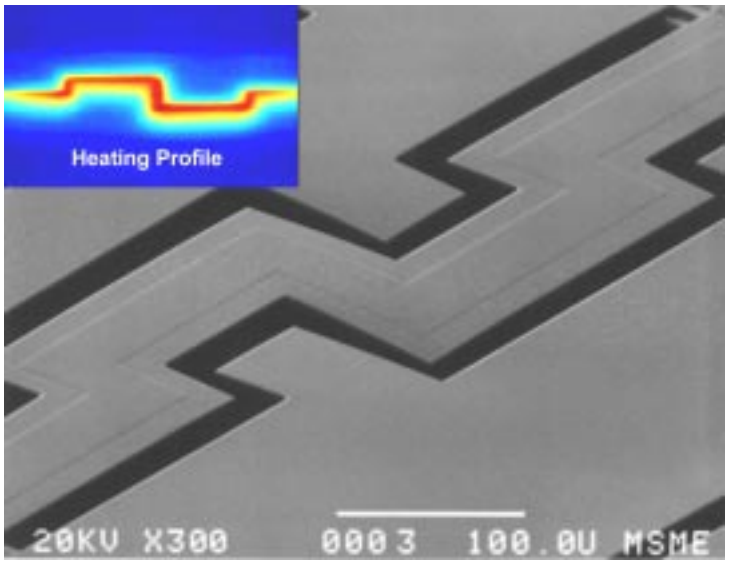

Figure 15. Polysilicon igniter suspended on an LSN membrane. Inset: measured heating profile at 8V, 2.6mA. Max temp = 182^{o}C

and n-poly were 30 Ohms/square and 15 Ohms/square, respectively. Functionality was once again demonstrated by placing fuel directly on the suspended heaters and increasing the dc voltage to the point of ignition. Ignition occurred with input voltages of approximately 25 V for p-doped poly and 15 V for n-doped poly. Although current was not directly measured, approximate power supply current outputs in the realm of 10-15 mA were observed at the time of ignition for both types of igniters. The total power supplied during ignition is then estimated to be 0.3 W for p-poly and 0.2 W for n-poly. By Ohm's Law, this implies that heater resistance approximately doubles, which is correlated to a temperature rise of 1000 K by the relation:

$$T = \frac{\left(\frac{R}{R_0}\right) - 1}{TCR} + T_0$$

where, T is temperature (K), T_0 is the initial or ambient temperature, R is resistance (W), R_0 is resistance at ambient temperature, and TCR is the thermal coefficient of resistance (1×10^{-3} K^{-1} for polysilicon). Properties for p-doped and n-doped igniters of the same design are summarized in Table 5. Because the n-doped polysilicon igniters are able to ignite the propellant using lower power than p-doped, they are preferred for this application. It should be noted, however, that the type of doping is used only as a convenient label for differentiating the two types of igniters fabricated, and it does not exclusively determine the functionality of the igniters. The n-poly igniters may be superior because they are thinner and have a lower resistance than p-poly igniters, allow-

ing increased heating at lower applied voltages. Further experimentation with doping levels and heater geometry might yield an even lower power igniter.

Property	P-poly	N-poly
Thickness [μm]	0.6	0.3
Resistance [kΩ]	1.1	0.6
$V_{ignition}$ [volts]	25	15
$P_{ignition}$ [W]	0.3	0.2

Table 5. Parameters for p-poly and n-poly Igniters

Igniter Time Constant

Igniters were tested with and without fuel loading to determine the time constant associated with resistor heating. The time constant reflects the time required by the heater to heat up once a voltage is applied, and is equivalent to the product of the thermal resistance and thermal capacitance. To determine the igniter's time constant, a step voltage was applied to the heater in series with a known resistor. By measuring the voltages across the heater and the series resistor, the current was calculated and used to determine heater resistance. Resistance values were correlated to temperature as discussed previously. The thermal time constant, τ, a function of the thermal resistance and thermal capacitance, can then be determined by correlating the data with:

$$\Delta T = a\left(1 - e^{-\frac{t}{\tau}}\right)$$

where, ΔT is temperature change (K), a is a constant reflecting the input power and thermal resistance, and t is time (s). Figure 16 shows the plots of igniter temperature rise versus time for a p-poly igniter with no fuel load and an igniter with a propellant-filled ceramic cylinder placed on it. The time constants are 4.6 ms and 3.8 ms, respectively. The temperature does not get as high with the fuel loading, likely because this increases the thermal conductance of the system. However, the temperatures reached in Figure 16 a and b for even the fuel-loaded heater are much higher than the 1000 K temperature rise estimated above. This may be because the propellant in the cylinder is not necessarily in direct contact with the igniter; whereas, in the previous test setup, propellant was placed directly on top of the igniter, ensuring good contact. Following the trend of increased thermal resistance with propellant loading, it makes sense that the temperatures estimated previously are lower than the measured temperatures. Increased thermal resistance implies that the thermal capacitance of the system was decreased by more than the thermal resistance increase in order to lower the thermal time constant by 16%.

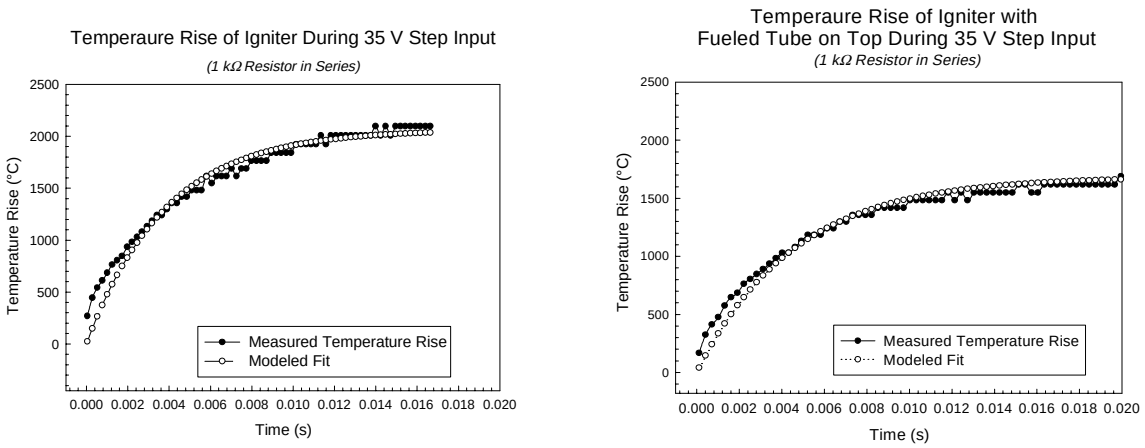

Figure 16. Temperature rise of a p-poly igniter a) without fuel loading (τ = 4.6 ms), and b) with ceramic tube filled with fuel on top of heater (τ = 3.8 ms)

Ignition Time Delay

Despite the millisecond time constant of the igniter, ignition does not occur quite so quickly. As discussed in 2.3, the igniter heat only begins the reactions that develop into all-out combustion. The total ignition time delay was measured using the thermopiles on the outer edges of the nozzle chip to determine the time of ignition, occurring sometime after a voltage is applied across the heater. Figure 17 a and b represent the range of time delays measured. In these plots,

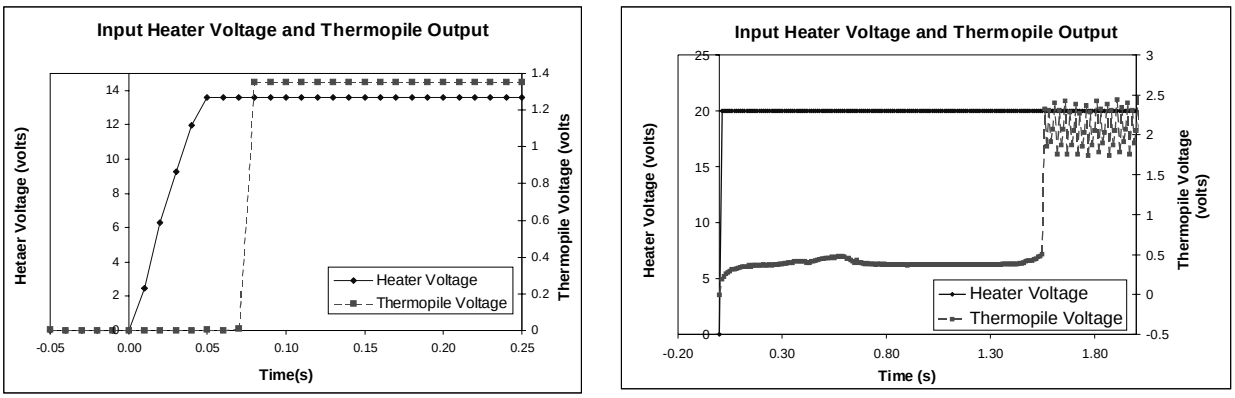

Figure 17. Input heater voltage and thermopile output are plotted to show the time between voltage applied to the heater and ignition. Post-ignition thermopile voltage magnitudes may be inaccurate due to signal coupling, but these plot do conclusively show a) a 0.02 s time delay and b) a 1.5 s time delay between the maximum applied heater voltage and ignition.

coupling between the thermopile output and supplied voltage was observed after ignition, implying that thermopile output values are inaccurate; however, the plots are still useful for determining the time and energy required for ignition, and since coupling begins at the time of ignition, the

time constant of the thermopiles need not be considered. Figure 17a indicates a time delay of approximately 0.02 s after the maximum heater voltage is reached. In Figure 17b, an initial rise in thermopile output is due to the heat generated on the chip. Ignition occurs 1.5 s after the heater voltage is applied. N-poly heaters were used in both cases. From the igniter power estimates given earlier, the total energy input to the system during ignition is anywhere between 4 mJ and 300 mJ. It is unclear why such a wide range of ignition time delays were observed. Possible explanations include varied doping and thickness of the polysilicon heaters due to process variations, nonuniformities in the propellant grain, or differing contact areas between the propellant and the igniter.

Propellant-Igniter Contact

A qualitative aspect of igniter performance that merits mention is that while igniter reliability and process yield is quite good, ignition can be difficult to achieve if the propellant grain is not directly touching the igniter. This means that in the assembly process, care must be taken to epoxy the ceramic combustion chamber to the igniter such that no air gap remains between the igniter and the propellant. One strategy that worked effectively is to loosely pack propellant bits at the nozzle end of the rocket, making it likely that at least a small bit of fuel touches the igniter, as in Figure 18. This method of assembly, however, often resulted in ruptured, non-functioning

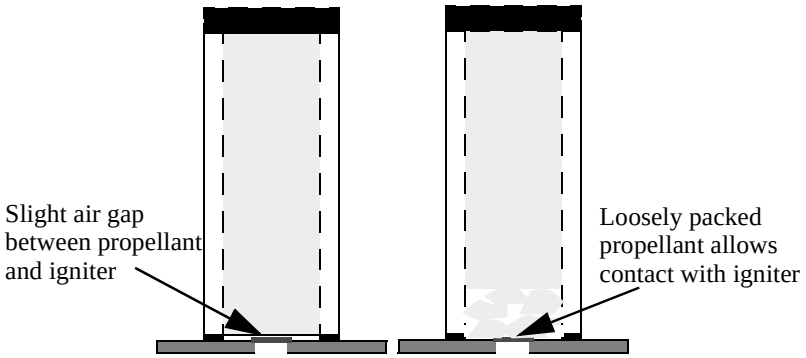

Figure 18. Illustration of the air gap between propellant grain and igniter. Loosely packing a small portion of the fuel helps ensure good contact, although sometimes results in rupturing the igniter membrane.

igniters. Ideally, a fabrication process in which the combustion chamber and nozzle could be bonded in wafer form, allowing the propellant to be loaded directly against the igniter before backside etching, is desirable.

5.2 Thrust

The most basic function of any rocket is to produce thrust. In order to quantify the amount of thrust generated by microrockets, a specially designed thrust measurement device was used. A description of the measurement device, testing results and analysis follow.

Measurement Set-Up

A thrust measurement device was designed and built to test microrocket thrust (Figure 19). The device operates by attaching the rocket to a rigid pendulum. A force sensor is placed so

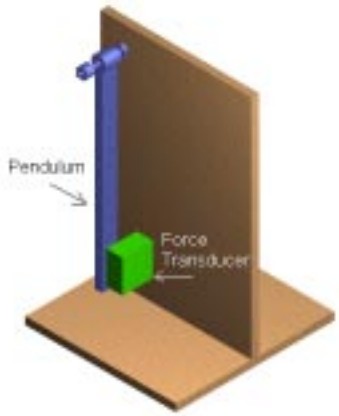

Figure 19 Thrust Measurement Platform

that it is touching the pendulum arm, and the output signal from the force sensor is monitored when the rocket is ignited. Thrust is determined using the moment equation governing the static pendulum:

$$\Sigma M_0 = F_r d_r - F_s d_s = 0$$

where, M_0 is the moment about the pendulum bearing (N-m), F_r is the force of the rocket (N), d_r is the distance of the rocket from the pendulum bearing (m), F_s is the force measured by the sensor (F), and d_s is the distance of the sensor from the pendulum bearing (m). Solving for F_r,

$$F_r = \frac{F_s d_s}{d_r}$$

Testing Results

Thrust measurements were performed on rockets with cylindrical ceramic combustion chambers and nozzles, as shown in Figure 20. Combustion chambers had inner diameters of 3.2 mm and lengths of either 12.7 mm or 25.4 mm. Ceramic tubes of outer diameter equal to combustion chamber inner diameter were used as non-diverging nozzles by inserting them into ceramic combustion chambers and epoxying into place. Nozzle throat diameters of 0.157 cm, and lengths of either 6.35 mm or 12.7 mm were used. A commercial hobby rocket wire filament igniter was used by inserting it through small holes in the combustion chamber near the nozzle or into the nozzle itself such that combustion began at the nozzle end of the rocket and burned through to the nose of the rocket.

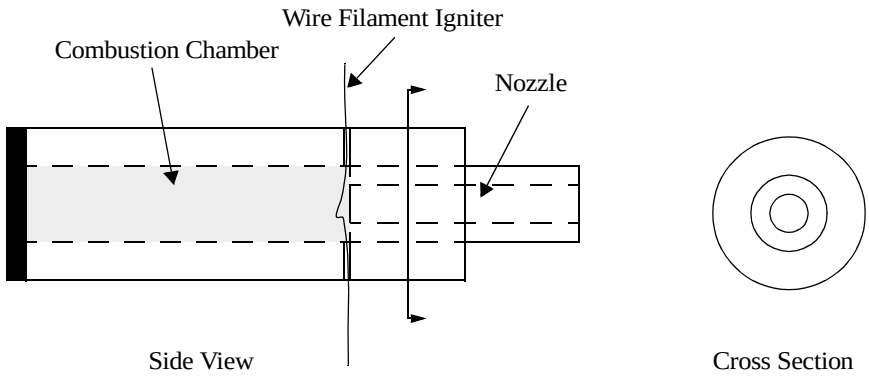

Figure 20. Side view and cross section of ceramic rockets used for thrust testing.

Despite the non-optimal nozzle and observations that some exhaust exited the igniter holes, thrusts peaking in the 4-10 mN range were routinely measured, and a maximum peak value of 15 mN was observed at atmospheric pressure and approximately 300 K. Figure 21 a and b show typical thrust curves for ceramic rockets with short and long-bodied combustion chambers, respectively. Figure 22 shows the highest measured thrust for a rocket of similar design. The combustion chamber lengths include only the portion of the chambers containing fuel, and the mass fraction displayed in these plots is equal to the ratio of propellant mass to the mass of the fueled rocket before ignition. In all cases, an initial peak was followed by a steady burn, which is commensurate with what might be expected for an end-burner propellant shape [12]. Results indicate that rockets with longer combustion chambers, and therefore more propellant, did not generally produce higher initial peak thrusts than shorter rockets, but they did sustain a low level of thrust for a longer period of time. This is to be expected because the shape of the thrust curve is largely a function of the variations in the surface area of fuel burning. Since both long and short combustion chambers had the same diameter and burned from end to end, thrust magnitudes were similar. Nozzle lengths did not noticeably impact thrust generation.

Overall, burn rates varied from 1 to 3 mms^{-1}, and seemed to be inversely related to the magnitude of the initial thrust peak. Since burn rate is very much dependent on chamber pressure and AP particle size and distributions, the wide range of burn rates were likely the result of variations in the propellant mixture, possibly coupled with varying combustion chamber leakage. Another conceivable possibility is that igniters were embedded further in some propellant grains than in others, causing more or less of the propellant grain to ignite during the initial peak. When a larger propellant area is ignited, a higher initial thrust peak is generated, leaving less propellant to combust and a higher chamber pressure and temperature to expedite burning.

Testing of integrated microrockets with cylindrical ceramic chambers and silicon nozzle chips yielded similar results to ceramic-only thrust testing. Again, an initial peak was observed,

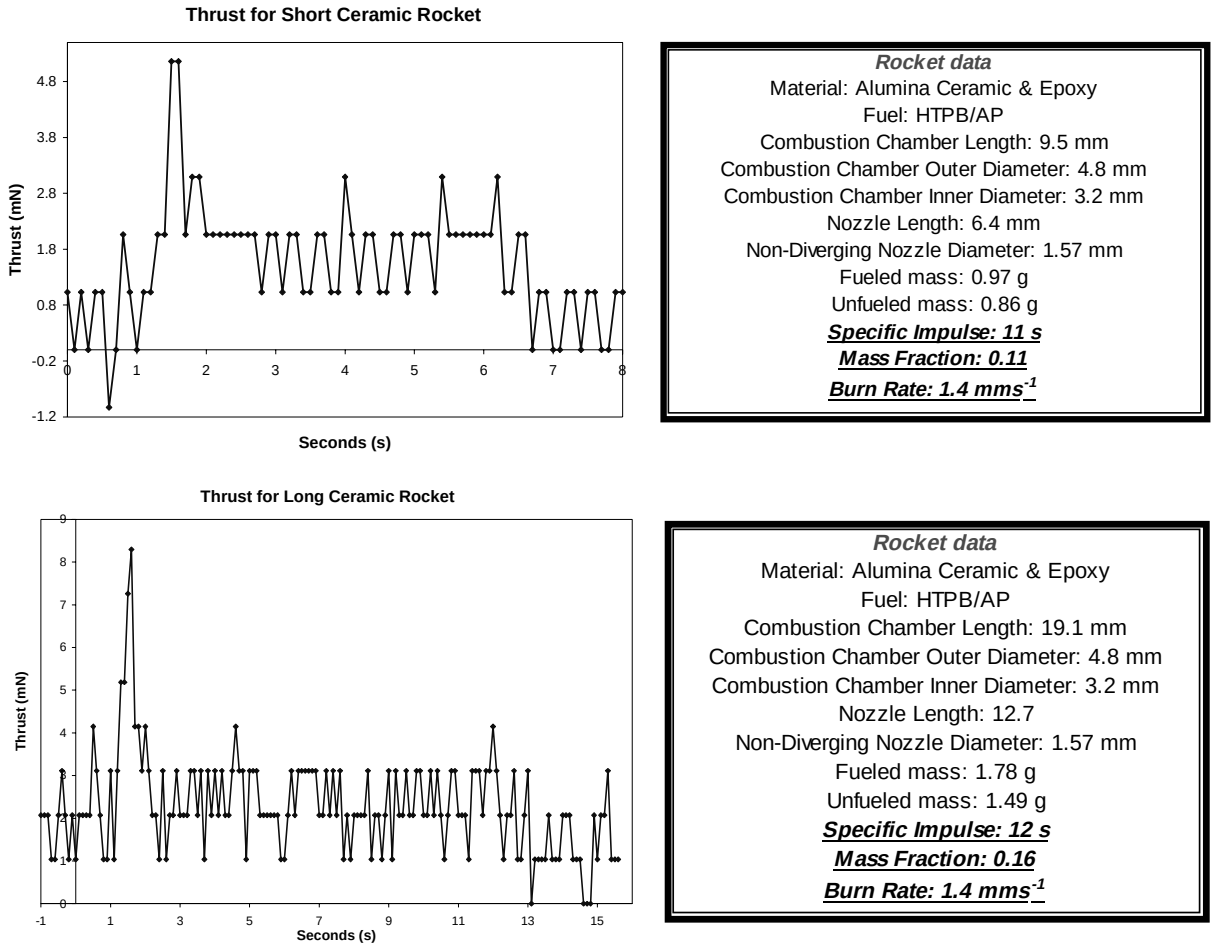

Figure 21. Typical ceramic rocket thrust curve for a) short and b) long combustion chambers.

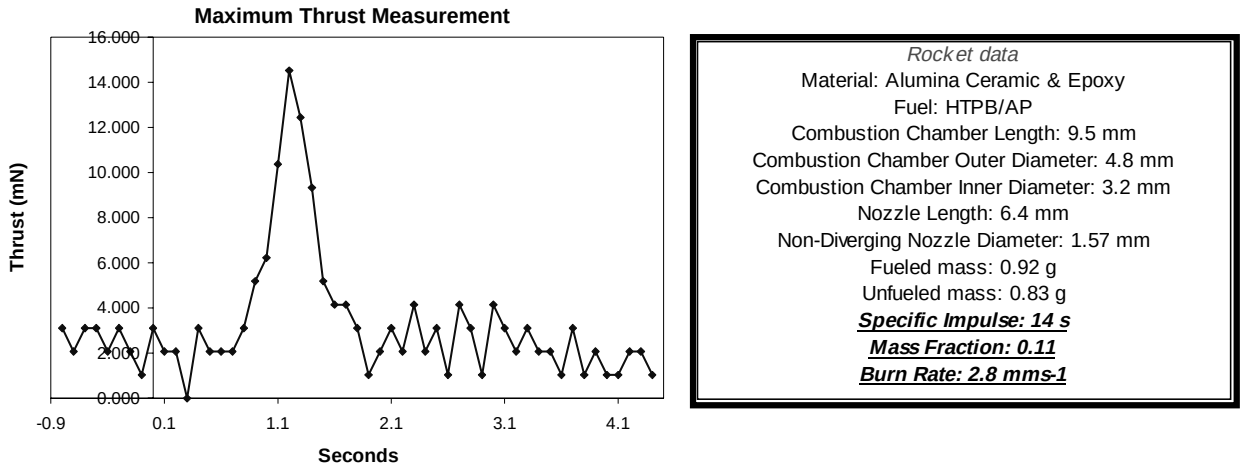

Figure 22. Thrust curve for ceramic rocket with maximum peak thrust of 15 mN.

followed by a steady burn, as shown in Figure 23. Although the thrusts generated are not high enough for most flight applications on the earth's surface, the low thrust may be well-suited to applications for space systems. Specifically, for the thrust curve in Figure 23, enough thrust is generated to accelerate the rocket's 0.75 g mass at 2.67 ms^{-2} for 7 s. Without the effects of gravity or drag, a velocity of approximately 20 ms^{-1} and distance of 65 m would be reached by the end of the burn.

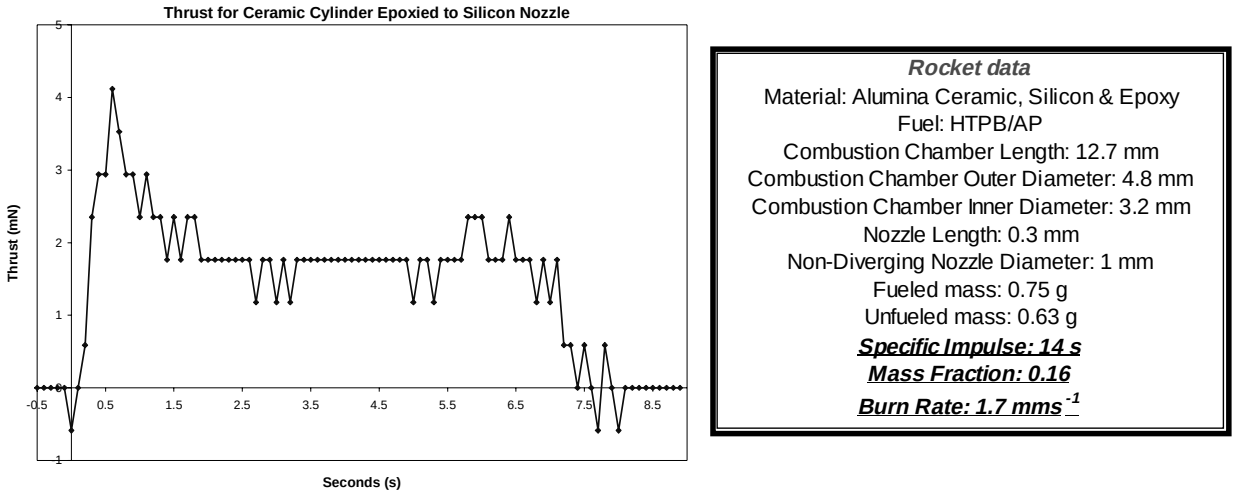

Figure 23. Thrust curve for integrated microrocket assembly: ceramic combustion chamber epoxied to silicon nozzle.

Comparison with "Explosive Propulsion"

In a best-case scenario given the measured thrust, less than 1 J is used to propel the rocket. For propellant that supposedly has an energy density of 5 kJg^{-1}, this leads to an abysmally low efficiency. Also, measured I_{sp} values are an order of magnitude lower than potential values for HTPB/AP propellant. For comparison, the thrust generated by a propellant-filled ceramic cylinder with epoxy sealing both ends was observed to be over 2 N. The cylinder was shorter, but of the same diameter as those mentioned previously (4.8 mm outer diameter, 3.2 mm inner diameter, 6.35 mm long). The exact thrust value is unknown as it exceeded the measurement capacity. One epoxy cap was completely blown off of the chamber (and impacted the tester with enough force to cause injury). Inside the remaining portion of the chamber, combustion continued until the propellant was exhausted. Analysis of the severed section of sealed rocket's epoxy indicates that a pressure of 130 atm was generated in the combustion chamber. Although this propulsion mechanism may more aptly be called explosive propulsion than rocket propulsion, high impulse projectiles can be fabricated, with thrusts proportional to the force required to break a sealant or membrane over the combustion chamber. The digital thrusters reported by Janson [5] operate in

this manner. In these devices, a membrane is broken directly following ignition, and fuel often exits the thruster nozzle uncombusted, meaning that the actual thrust mechanism is not rocket propulsion but breaking a membrane explosively.

This study suggests that explosively generated thrusts can reach over two orders of magnitude greater than conventional thrusts of microscale rockets; however, the specific impulse is not necessarily enhanced since the high thrust value is sustained for only a fraction of a second during the "explosion." Assuming that optimized nozzle geometry could improve performance over a non-diverging nozzle by the same factor as for larger nozzles, thrust could be expected to double or perhaps triple in magnitude. Perhaps more appropriate is increasing the propellant mass fraction of the rocket by reducing overall rocket mass in order to achieve flight. For the thrusts reported, a fourfold reduction in the unfueled rocket mass would enable flight on earth.

Calculated Performance Potential

A reduction in rocket mass and optimized nozzle geometry are viable ways to enhance the flight capacity of the microrockets presented. Here, microrocket performance parameters are calculated and plotted as a function of cylindrical ceramic combustion chamber thickness. The mass of the rocket is assumed to be made up entirely by the combustion chamber and the fuel.

Cylindrical ceramic combustion chambers are analyzed as thin-walled pressure vessels to determine the pressure in the combustion chamber. Tensile stress on the vessel is maximum in

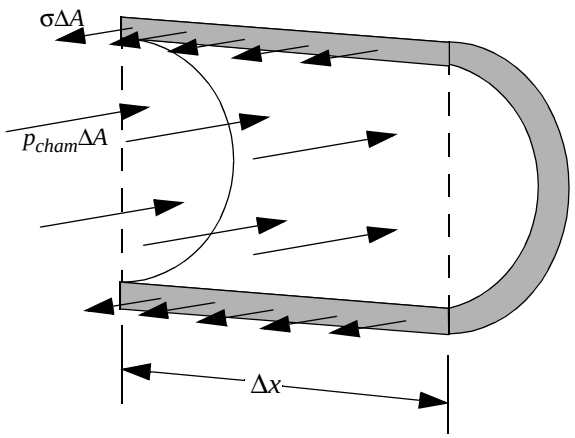

Figure 24. Section of cylindrical vessel depicting hoop stress (σ) balanced by chamber pressure.

the circumferential direction. The stress in the chamber walls, known as hoop stress (σ), is depicted in Figure 24 and given by to following equation:

$$\sigma = \frac{p_{cham} r}{t}$$

where, p_{cham} is the pressure inside the chamber (N/m^2), r is the radius of the cylinder (m), and t is the wall thickness (m). Given that alumina ceramic has a flexural stress of 250 MPa at 1100 K, the maximum chamber pressure can be found for varying wall thicknesses, having a constant radius of 1.6 mm.

Once the maximum chamber pressure is calculated, the nozzle exit velocity is computed for an optimal nozzle (pressure at nozzle exit = atmospheric pressure) by [11]:

$$c = \sqrt{\left[2\frac{k}{(k-1)}\right]RT\left[1-\left(\frac{p_{atm}}{p_{cham}}\right)^{(k-1)/k}\right]}$$

where, k is the specific heat ratio of the exhaust gases, R is the ideal gas constant, T is the combustion chamber temperature (K), and p_{atm} is atmospheric pressure (Pa).

The burn rate, r, is then given by [11]:

$$r = ap_{cham}^{n}$$

where, a is a constant influenced by ambient grain temperature, and n is the burning rate pressure exponent. Dividing the length of the chamber by the burn rate, the total burn time is determined. From this, the propellant mass flow rate is found by:

$$\dot{m} = \frac{m_{fuel}}{burn\ \ time}$$

where, m_{fuel} is the total propellant mass, assumed to be 0.1 g. Finally, thrust, F, is the product of the mass flow rate and the exhaust velocity, and acceleration is given by F/m_{fuel}, and I_{sp} is computed as discussed in section 2.1.

Figure 25 is a plot of propellant mass fraction, chamber pressure, thrust, specific impulse, and acceleration for a range of combustion chamber thicknesses. This plot illustrates the trade off between combustion chamber strength and mass. When the combustion chamber mass gets very low and the mass fraction approaches 1, only very low pressures can be withstood such that thrust and I_{sp} are also low. At the high pressures generated when the combustion chamber walls are thick, the relatively high mass of the rocket limits acceleration. Maximum acceleration is achieved when the propellant mass fraction is approximately 0.6 and 40 mN of thrust are produced. I_{sp} is computed to be 34 s at this wall thickness, and continues increasing slowly to near 40 s. These values indicate that microrocket flight is, indeed, feasible with accelerations nearing 25g, which is on the order of the acceleration of an air-launched missile.

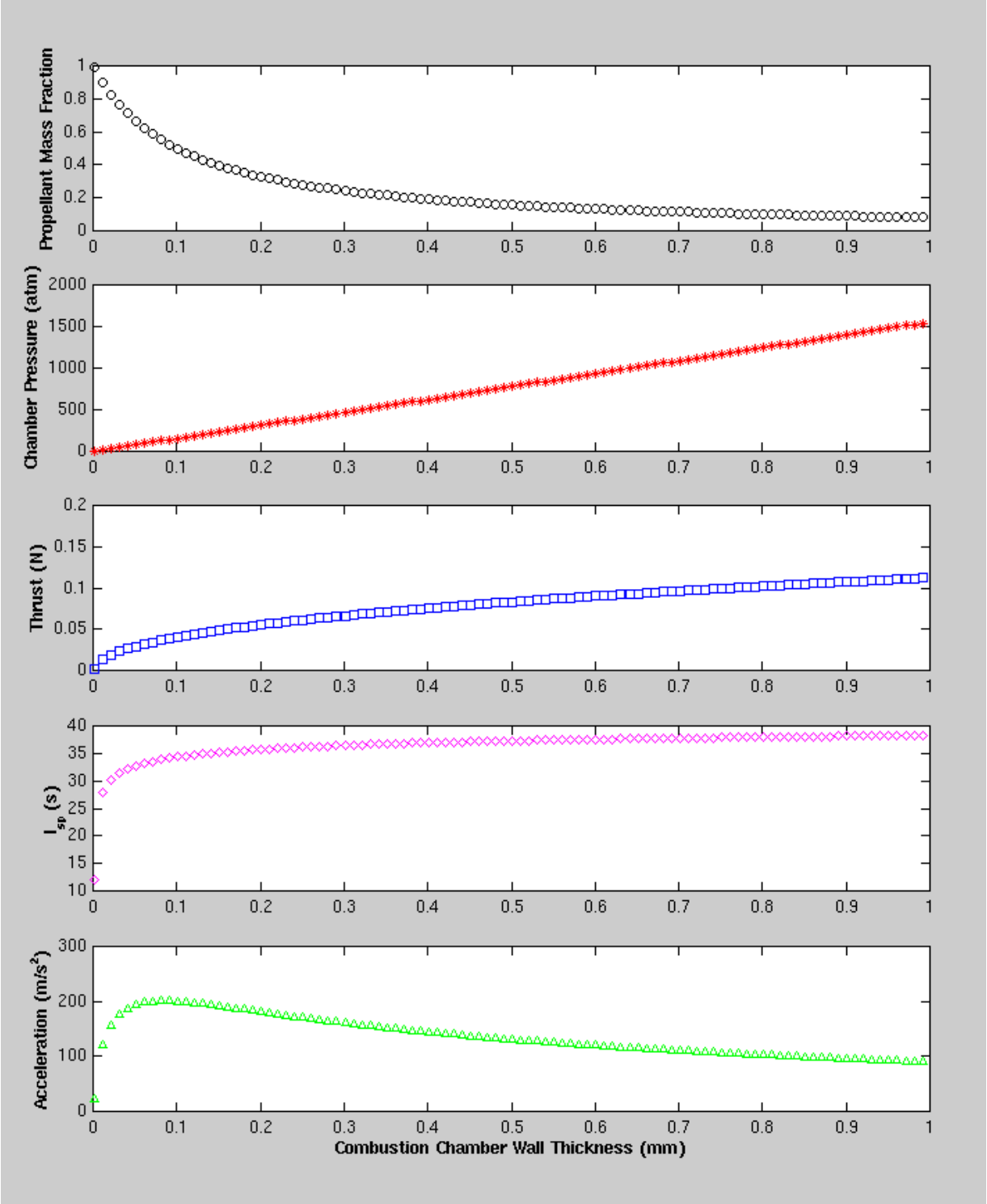

Figure 25. Propellant mass fraction, maximum allowable chamber pressure, thrust, I_{sp}, and acceleration calculated based on alumina ceramic combustion chamber wall thickness. $a=2x10^{-5}$, $n=0.4$, $k=1.3$, $T=2000K$

6. Power Conversion

While the goal of creating a MEMS rocket is to convert combustion energy into thrust, it is impossible to avoid thermal losses in the system due to the large surface area to volume ratio inherent in sub-centimeter scaling. Therefore, one can conceive of recovering this thermally stored power locally, or "on board" the rocket to form a fully integrated rocket system with electrical power generation.

Combustion reactants are plausible MEMS power sources due to their high energy density in comparison to most other energy storage methods, such as electrochemical cells and elastic strain energy. Additionally, solid propellants do not require a complex system of storage tanks and valves, making them a more feasible power source than liquid propellants, for which the necessary handling volume often outweighs the advantage of compact energy storage [10]. Composite propellants have the disadvantages of needing initial power input for ignition and having a continuous, non-adjustable combustion once ignition has occurred. Otherwise stated, the propellant grain is exhausted completely once ignited. Due to these drawbacks, solid propellants may be unsuited to long-term, power-consumptive applications. Power generation during the flight of a microrocket, however, could potentially be useful for MEMS control surface actuation or operating payload circuitry.

A thermal gradient of potentially hundreds or even thousands of degrees can exist between the combustion flame front and the outer edges of the rocket. The total available energy in the microrocket system is the propellant energy plus the input ignition energy. Considering the ignition energy negligible compared to combustion energy, 500 J are produced by burning 0.1 g of 5 kJg^{-1} propellant. Only a small fraction of this energy is converted into kinetic energy to move the rocket, while much of it is dissipated as heat. Therefore, a thermal gradient of potentially hundreds of degrees centigrade can exist between the combustion flame front and the outer edges of the rocket. Thermocouples are often used as thermal sensors because they convert temperature differences into proportional voltages. The thermoelectric effects that govern this type of thermal conversion combined with the ability to fabricate them in a surface micromachining process make thermopiles, or multiple junction thermocouples, useful energy converters for microrockets.

6.1 Thermoelectric Effects

Thermoelectric effects govern the material properties relating temperature and electrical characteristics. These include the Seebeck effect, the Peltier effect and the Thomson effect.

Seebeck Effect

The thermoelectric effect discovered by Seebeck in 1826 addresses the material property of electrical conductors and semiconductors to convert a temperature difference into an electrical

potential, or Seebeck voltage (V_s). When two different conductors are in contact in a hot region (T_h) and the unconnected ends remain at a lower temperature (T_l), the Seebeck voltage generated is related to the temperature difference by [17]:

$$V_S = \int_{T_l}^{T_h} \alpha_a(T) dT + \int_{T_h}^{T_l} \alpha_b(T) dT$$

where α_a and α_b are the Seebeck coefficients for conductors *a* and conductor *b*. The Seebeck coefficient of a conductor is usually given in units of μV/K or mV/K. Such a device, with two legs of different conducting materials, is called a thermocouple.

The Seebeck coefficient of a given material varies with temperature, but it can be considered constant for small changes in temperature, when $(T_h\text{-}T_l)/T_l << 1$. In this case, the Seebeck voltage of a thermocouple is given by:

$$V_S = (\alpha_a - \alpha_b)\Delta T = \alpha_{ab}\Delta T$$

where α_{ab} is the relative Seebeck coefficient (μV/K).

Although the voltage generated by a single thermocouple is optimally only a few millivolts, a thermopile of *N* thermocouples in series will generate *N* times the voltage output of one thermocouple (Figure 26).

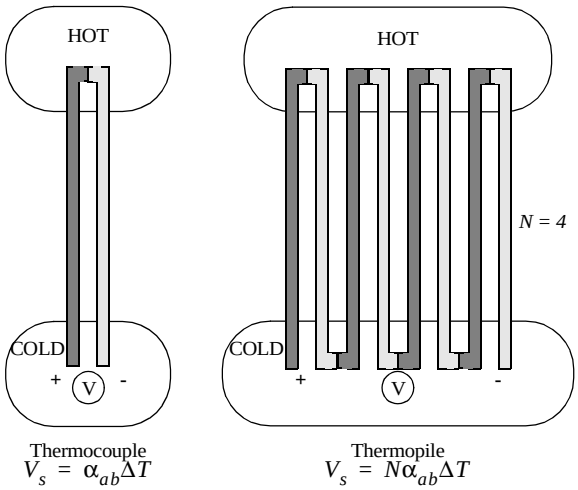

Figure 26. Thermocouple and N-junction thermopile. Up to N times the voltage of a single thermocouple can be generated by an N-junction thermopile.

The Seebeck coefficient is a bulk material property, and it is a function of the material's Fermi energy, which depends on carrier concentration, carrier effective mass, and temperature. The gradient in the Fermi energy, E_F, over the elementary charge, *q*, is proportional to the applied temperature gradient with the Seebeck coefficient as the constant of proportionality, as given by [18]:

$$\frac{\nabla E_F}{q} = \alpha \nabla \dot{T}$$

Three primary effects contribute to the generation of a Seebeck voltage in non-degenerate silicon [18]. First, the Fermi level shifts towards the middle of the band gap as temperature increases and the silicon becomes more intrinsic. Second, a charge build-up on the cold side of the semiconductor occurs due to the increased carrier velocity with increased temperature. Lastly, the temperature differential induces a net flow of phonons from hot to cold, dragging charge carriers toward the cold side. This occurs in the temperature region of approximately 10-500K, when momentum is transferred from phonons to charge carriers. Combining these effects, the expression for the Seebeck coefficient can be written as:

$$\alpha_i = \pm\frac{k}{q}\left(\ln\left(\left(\frac{N(T)}{n_i}\right) + \frac{5}{2} + s_i + \phi_i\right)\right)$$

where, k is Boltzmann's constant, q is elementary charge, n is the electron density, s and ϕ describe the effects of carrier scattering and phonon drag, and $i = e$ or h, to denote electron or hole transport, indicating n-type and p-type materials, respectively. Similarly, N, a function of temperature, is the conduction band energy state density for n-type materials or the valence band energy state density for p-type materials.

In general, the absolute value of the Seebeck coefficient increases logarithmically with the resistivity, and it also increases, although not linearly, with increasing temperature. In metals, there is no band gap, and the Seebeck coefficient varies linearly with temperature.Advances in mechanical microsensor fabrication in MEMS and CMOS technologies [17],[19] make the integration of thermal converters in a microrocket assembly possible. Seebeck coefficients have been characterized for standard CMOS conductors [19]-[22]. The highest relative Seebeck coefficient for the ORBIT 1.2 μm process is 785 μV/K for n-poly/p^+-active layer thermocouples[22].

The Seebeck coefficient is a positive value for materials in which holes dominate conduction, as in p-type materials, and negative where charge is transported by electrons, as in n-type materials. The relative Seebeck coefficient determines the voltage generation of a thermocouple, implying that combining a p-type leg with an n-type leg will achieve the largest voltages. Furthermore, although a potential is generated whenever a thermal gradient is maintained from one end of the sample to the other, two legs of the same material will not produce any voltage due to symmetry.

Figure of Merit

Although respectably large voltages can be reached by thermocouple materials with high relative Seebeck coefficients, often those same materials have high resistivity and high thermal conductivities, which decreases overall thermal conversion efficiency. It is then convenient to define a thermoelectric figure of merit, *Z*:

$$Z = \frac{\alpha^2}{\rho k}$$

where, α is the Seebeck coefficient, ρ is resistivity and *k* is thermal conductivity. Therefore, materials with high Seebeck coefficients, low electrical resistivity and low thermal conductivity make the most efficient thermal power converters. Among semiconductors, doping levels with carrier concentrations around 10^{19} cm $^{-3}$ produce the highest *Z* values [17].

The optimal figure of merit for a thermocouple depends on the geometry of the thermocouple, and is obtained under the following condition:

$$\left(\frac{A_b}{A_a}\right)^2 = \frac{\rho_b k_a}{\rho_a k_b}$$

where, A_a and A_b are the cross sectional areas of the two legs. The figure of merit for an optimal thermocouple can then be expressed by [19]:

$$Z_{opt} = \frac{\alpha_{ab}^2}{\left(\sqrt{\rho_a k_a} + \sqrt{\rho_b k_b}\right)^2}$$

In the following analysis, the Seebeck coefficient of the fabricated thermopiles is the primary thermoelectric property that will be discussed. It is important, however, to be aware of the other effects in determining the thermopile materials for optimal performance. Milanovic *et al* discuss simulation and measured values based on Seebeck, Peltier and Thomson thermoelectric effects in [23].

Thermal Time Constant

The thermal time constant is, in essence, the response time of the thermopile. It describes how fast the output of the thermopile responds to the change of an input signal. For a step input having power *P*, the thermal time constant, τ, can be determined using [19]:

$$\Delta T = \frac{P}{G}\left(1 - e^{-\frac{t}{\tau}}\right)$$

where, G is the total thermal conductance between the heater and the heat sink. Applied to a microrocket thermopile, the thermal resistances of the silicon, thermopile, air cavities and heater by means of conduction, convection and radiation must be included in G.

The thermal time constant can be calculated as the product of the thermal capacitance, C_t, and the thermal resistance, R_t, as given by:

$$R_t = \frac{L}{kA} \qquad C_t = c_p \rho V$$

where, L is length (m), k is thermal conductivity ($Wm^{-1}K^{-1}$), A is area (m^2), c_p is specific heat capacity ($Jkg^{-1}K^{-1}$), ρ is material density (kg/m^3), and V is volume (m^3). The thermal time constant and the ultimate temperature differential over the thermopile are related to the thermal conductivity of the donut-shaped region where the thermopiles are located. By decreasing the thermal conductivity in order to increase the temperature differential, the thermal time constant will increase. This can be done by eliminating much of the silicon present in the thermopile ring area since silicon has a much higher thermal conductivity than air. In Figure 27, the thermal time constant is plotted versus % silicon inthe thermal isolation ring. Only conduction in this ring is considered. The fabricated nozzle ring is about 12% silicon. Therefore, the predicted time constant for just the thermal isolation ring is about 25 ms.

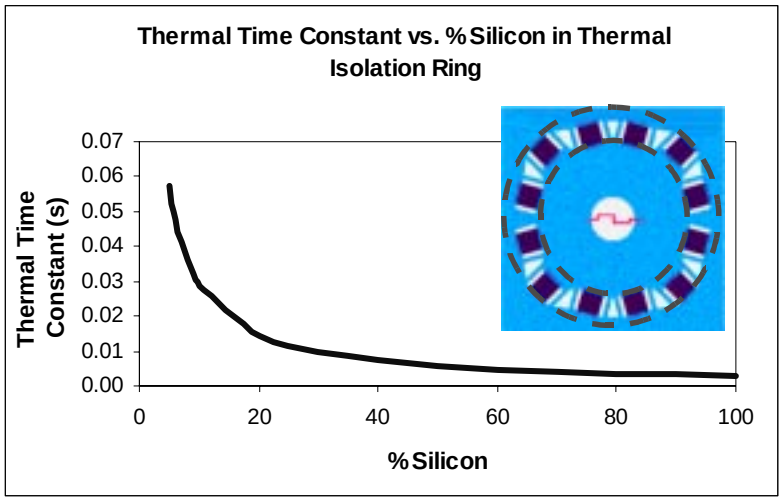

Figure 27. Thermal time constant change with % silicon in the thermal isolation ring, a series of backside-etched cavities. Thermal isolation ring is outlined by dashed line.

6.2 Simulation

Ultimately, the temperature differential between the hot and cold junctions of the thermopile will determine the expected voltage generation. In order to get an estimate of the temperature distribution on the silicon nozzle chip for various configurations of etched thermal isolation cavi-

ties in the thermal isolation ring, simulations were performed using MEMCAD^{TM} thermal modeling tools. MEMCAD^{TM} uses finite element and boundary element solvers to determine properties of meshed structures. While used mainly as a design tool to determine the best configuration of holes in the silicon for maximum power generation, the simulated temperature distribution can be used as a baseline for determining expected thermopile performance. Only the silicon portion of the nozzle die was modeled since it is assumed that most of the heat transferred to the outer edges of the die will be through the silicon. Some heat transfer through the thermopile legs and LSN membrane is expected, but it does not effect the comparison of thermal isolation hole patterns in the silicon.

As an approximation of steady-state rocket flight conditions, a constant temperature of 1000 K was applied to the interior of the nozzle with an ambient air flow of $1x10^{9}$ μms^{-1} at 300 K over the rest of the silicon surface. Simulations were run for no thermal isolation cavities, cavities only under thermopiles, cavities under thermopiles with additional large holes and cavities under thermopiles with additional small holes. The same total volume of silicon was removed for the additional large holes and the additional small holes cases.

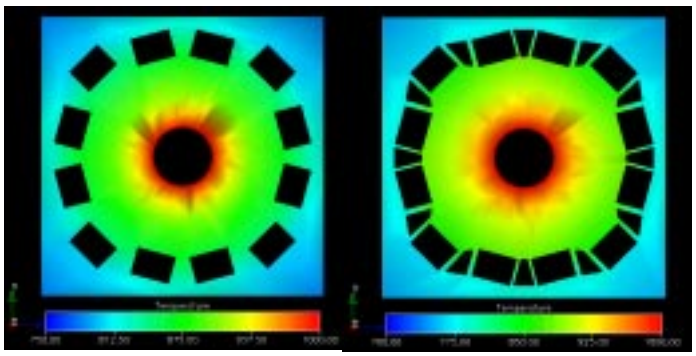

Figure 28. Simulated temperature distribution over a 5 mm square die for left) holes only under thermopiles and right) additional large holes.

Simulated temperature profiles over the silicon surface of 5 mm square die for the case having holes only under thermopiles and the case with additional large holes are shown in Figure 28. Anomalies near the nozzle are the result of meshing irregularities. As a more qualitative comparison of the different models, the plot in Figure 29 shows temperature distributions along the silicon surface starting from the nozzle and progressing upward toward the top of the die. From the plot, it is clear that increasing the volume of holes around the thermal isolation ring results in larger temperature differentials from one side of the ring to the other. The size of the thermal isolation holes does not seem to be much of a factor, which becomes apparent given that the same total hole volume is removed in the additional large and small hole cases and both result in similar temperature differences. The maximum steady-state temperature difference between

the hot side of the thermopile and the cold side of the thermopile is approximately 125 K for both added hole models. Based on these simulation results, the design with holes under thermopiles and additional large holes was used for fabrication.

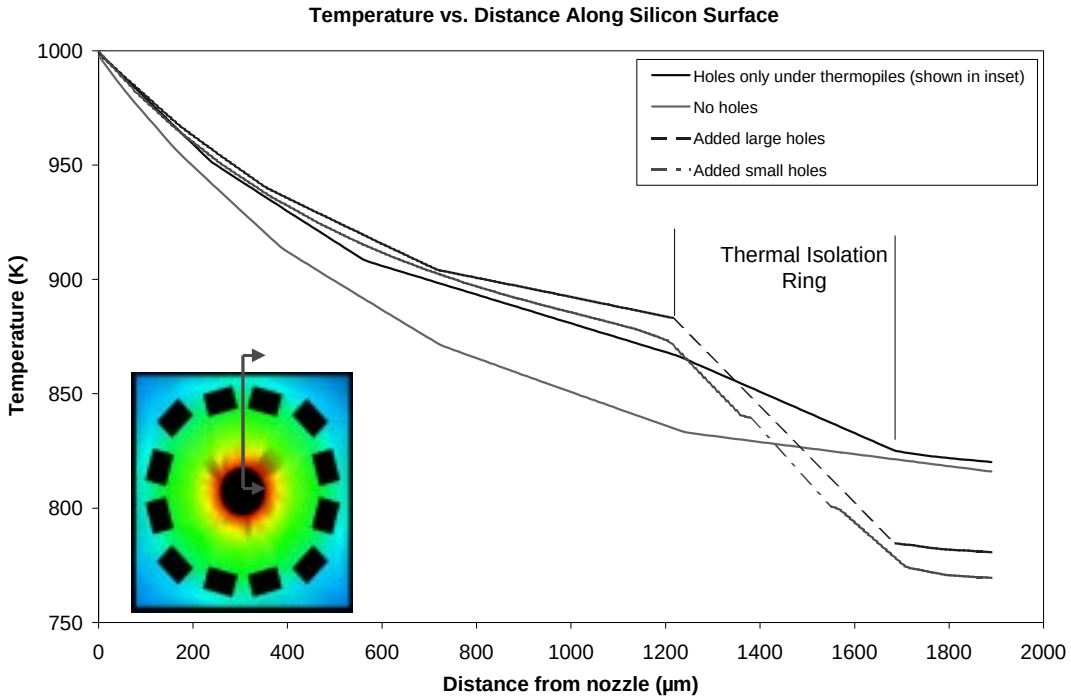

Figure 29. Plot of temperature vs. distance along silicon surface. Various hole configurations in thermal isolation ring are compared.

6.3 Thermopile Testing

10-junction thermopiles were fabricated using the process illustrated in Figure 12. Three thermopile material combinations were used: n-poly/p-poly, n-poly/aluminum and p-poly/aluminum. For each material combination, thermopiles were placed either spanning thermal isolation cavities or with the cold junction suspended over the cavity. A comparison of the three thermopiles and suspended versus non-suspended thermopiles was conducted to determine which one is the most efficient thermal power converter. Thermopile time constants were measured as well as voltages during propellant combustion. The micrograph in Figure 30 is an example of a suspended 10-junction n-poly/aluminum thermopile.

Determining the Best Thermopile Materials and Positioning

Thermopiles made up of ten thermocouple junctions were fabricated and tested on chips without nozzle holes, such that the polysilicon heater was heating the silicon substrate directly, as shown in Figure 31. Figure 32 a and b show the voltage and power thermopile output plotted versus input heater power for each thermopile material. P-poly/n-poly thermopiles generated the

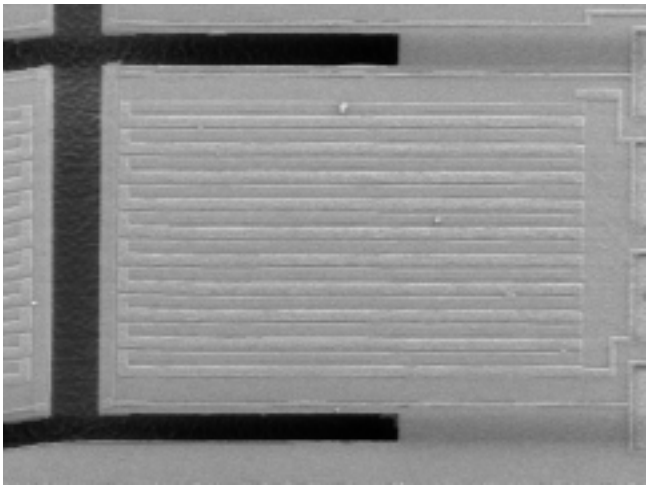

Figure 30. N-poly/aluminum 10-junction thermopile suspended on LSN membrane.

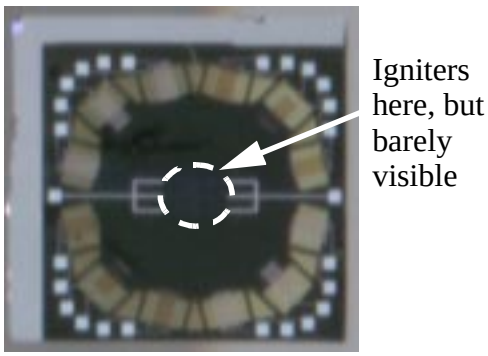

Figure 31. Silicon nozzle die with no nozzle etched. Igniters in the center of the die heat silicon surface directly for thermopile testing.

highest voltages and the highest power over the entire range of heater inputs. Since the power dissipated in the heater is linearly related to it's temperature rise, it also becomes clear that Seebeck voltages rise linearly with heater temperature. By measuring the resistance rise in the heater as power dissipation increases, the temperature can be calculated as discussed in 5.1. In Figure 32, 200 mW of heater power corresponds roughly to a 70 K heater temperature rise.

Figure 33 shows a comparison of power output for suspended and non-suspended thermopiles; suspending cold junctions over thermal isolation cavities was found to degrade performance for all material combinations. P-poly/n-poly data is plotted.

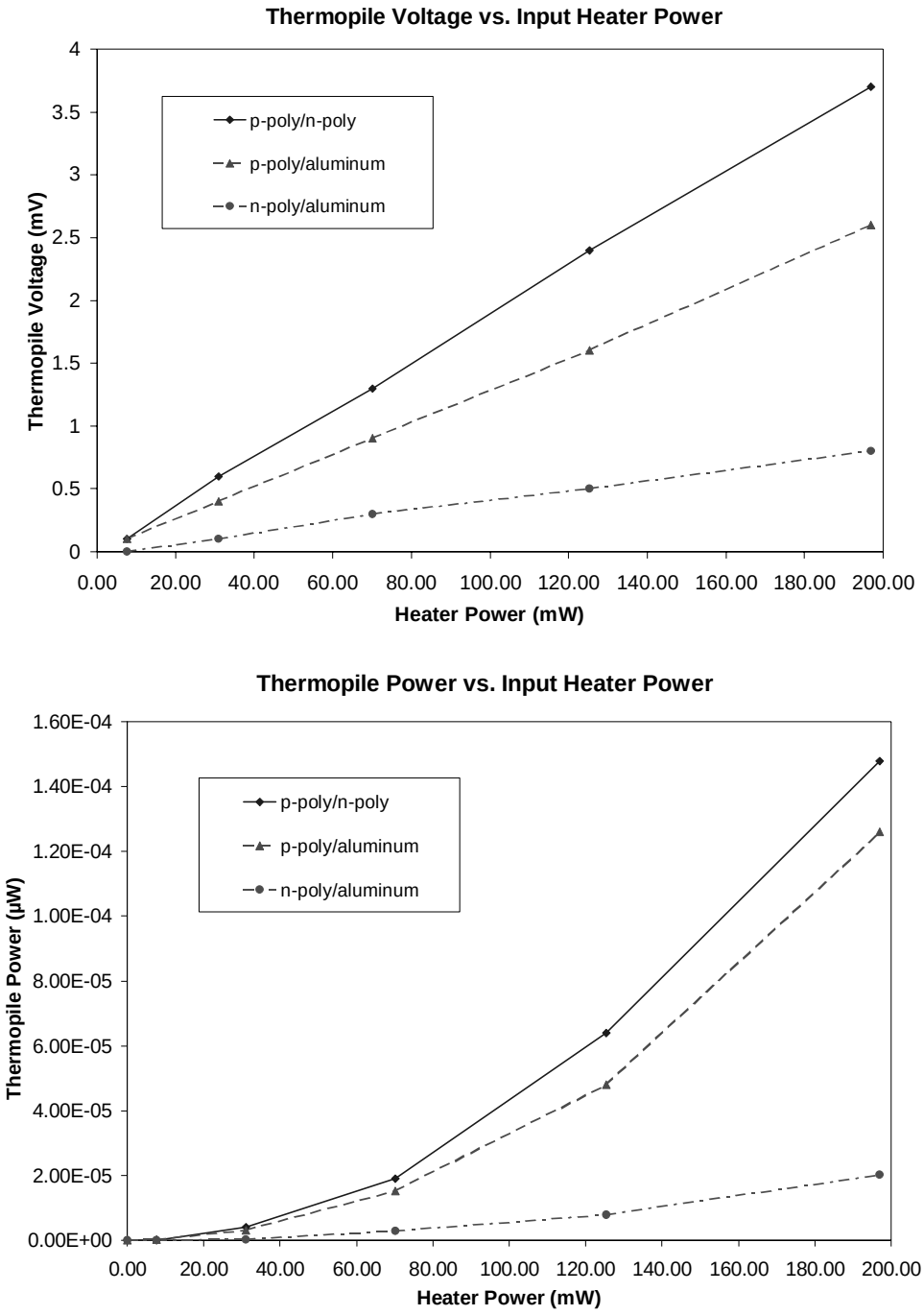

Figure 32 Plots of a) thermopile voltage output and b) thermopile power output vs. input heater power

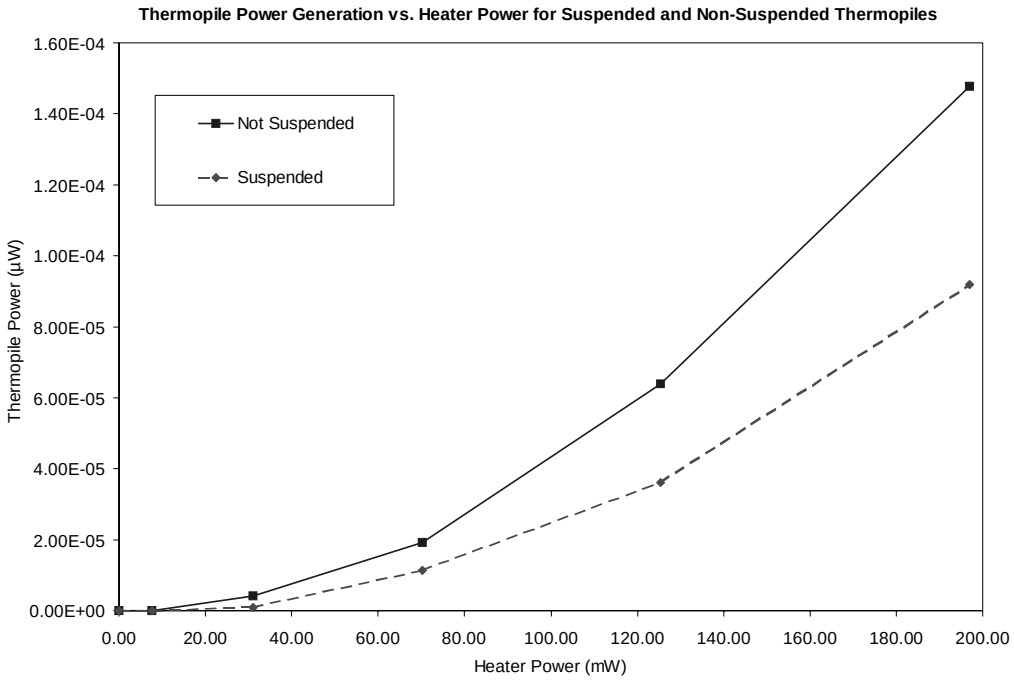

Figure 33. Comparison of power output for suspended vs. non-suspended p-poly/n-poly thermopiles (plotted against heater power).

Measured Time Constant

Using similar test die with no nozzle hole etched, the thermal time constant of the thermopiles was measured. While supplying a step input to the heater, thermopile output voltage was monitored. Increasing thermopile voltage outputs for 0.4 s, 1 s and 2 s input pulses at 100 V are shown in Figure 34 a-c. Although the time constants tend to increase with increasing pulse length, the modeled fit becomes worse. It suffices to say that thermopiles sensing a heat source in the center of the chip have a time constant in the realm of 0.1 s. Since this value is much smaller than the microrocket burn time, it can be assumed that a steady-state condition is reached during combustion, making the simulated temperature distributions applicable for the majority of the burn. The 0.1 s thermopile time constant is also much larger than the 25 ms predicted for the thermal isolation ring only, meaning that the heating of the center portion of the chip and of their thermopile structure itself contribute significantly toward increasing the time constant.

Performance During Combustion

Correlating the 70 K heater temperature increase linearly with the 700 K simulated temperature differential from nozzle to chip edge, a 12.5 K temperature differential between the hot and cold side of the thermopile can be assumed. This corresponds to a Seebeck coefficient of 320 µV/K for p-poly/n-poly 10-junction thermopiles (32 µV/K per thermocouple), about 4% of the

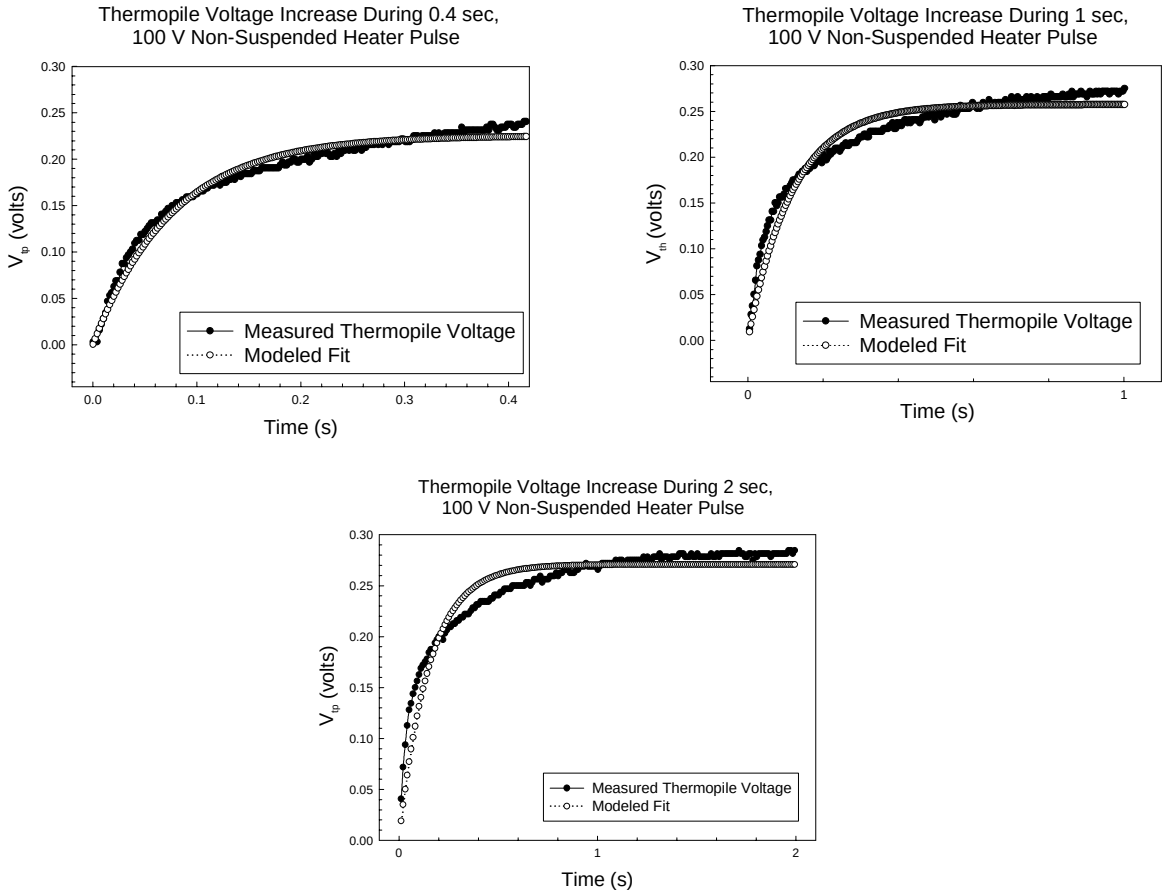

Figure 34 Thermopile Voltage Output after 100V input to heater of pulse length a)0.4 s, b)1.0 s, and c)2.0 s. Time constants are 0.076 s, 0.119 s, and 0.152 s, respectively.

maximum reported values. Assuming a more optimal Seebeck coefficient of 785 μV/K for a p-poly/n-poly thermocouple junction and a 10-junction thermopile resistance of 50 kOhms and that each chip has 12 such thermopiles, nearly 12 V and 60 μW could potentially be generated on a nozzle chip with a 125 K temperature differential. For a 7 second burn, this amounts to about $9x10^{-7}$ of the total energy of the rocket system. However, with HTPB/AP flame temperatures capable of reaching over 3000 K, the simulated steady-state 125 K temperature differential can be considered quite conservative.

Thermopile voltages were monitored during combustion occurring on the nozzle die (with ignition performed by the polysilicon igniter). Sustained voltages of over 1.2 V per p-poly/n-poly 10-junction thermopile were observed during combustion. By placing a resistor of known resistance in series with the thermopile, 10-junction thermopile power output was measured with maximum values of 10-20 μW. This value is higher than the most optimistic predictions, likely because the temperature differential generated across the thermopiles is much larger than

expected. For an array of 12 10-junction thermopiles, hundreds of microwatts could be generated, which would certainly be adequate to drive low-power CMOS circuitry.

One difficulty encountered in drawing power from thermopiles is that as a thermopile's voltage output increases, its resistance does as well, making it difficult to optimize power output for the entire burn time. Further experimentation is needed to determine the optimal load on a thermopile during operation.

In the rocket design presented, the nozzle die is considered fully populated with thermopiles when twelve 10-junction thermopiles are on the die. Increasing the number of thermocouple junctions placed around the rocket by making thinner legs, packing thermopiles more densely or using multiple tiers of thermopile rings is possible. This could potentially lead to much higher power output at the expense of more die surface dedicated to thermopiles.

7. Recommendations and Conclusions

In this body of research, a complete microrocket system has been presented. Although components are not optimally designed, functionality is demonstrated and measured results presented. Microrockets of mass less than 1 g are capable of producing thrust as high as 15 mN for nearly half of a second, with burn rates of 1-3mms^{-1}. Steady thrusts of approximately 2 mN have also been observed for several seconds. A microfabrication process for producing a microrocket nozzle integrated with polysilicon igniters and thermal power converters with backside-etched thermal isolation cavities has been completed. Ignition of HTPB/AP propellant by polysilicon resistive heaters has been demonstrated with power consumption as low as 0.2 W. Thermopiles were fabricated in the same process; n-poly/p-poly thermopiles generated the highest voltage and output power of those tested. Performance during microrocket operation indicates that for a 1 g rocket, hundreds of microwatts could be generated at nearly 12 volts by a rocket in flight for upto 7 seconds. Generalized conclusions and recommendations for improvement are stated below.

7.1 Propellant

HTPB/AP is an adequate microrocket propellant, with improved burning through small cross sections when AP particle size is decreased. Adding Al powder to the fuel is not appropriate for microrockets, as Al particles combust outside of a millimeter-scale combustion chamber and often clog sub-millimeter nozzle openings.

7.2 Fabrication

Cylindrical ceramic combustion chambers offer an advantage over 2-D combustion chambers fabricated in metal or silicon due primarily to lower thermal conductivity and better geometry for containing high pressures. Further investigation of combustion chamber geometries

should be performed, however, in order to decrease the mass of the system while maintaining thermal insulation and structural robustness. Integrating combustion chamber fabrication with nozzle fabrication would result in bulk fabrication and low-cost microrockets. To do this, micromachinable combustion chamber materials could be aligned with and bonded to silicon nozzles as part of the fabrication process.

Microprocessing techniques can be used successfully to integrate polysilicon resistive heating igniters and thermopile structures for power generation with micronozzles on silicon chips. Nozzle geometries remain to be optimized. One strategy for this is to control DRIE process parameters in order to form nozzles of varying geometries.

7.3 Ignition

Successful ignition by means of a resistive polysilicon heater suspended in an LSN membrane has been demonstrated, with a minimum input power of 0.2 W. Heater temperature can increase by more than 1000 K during this process. Further investigation of alternative ignition methods and their integration with microfabrication processes might result in lower power or more robust ignition mechanisms.

7.4 Thrust and Flight

Thrust is generated by the proposed microrocket system, but not enough for flight on earth. Nozzle optimization should result in significant increases to microrocket thrust. Lower microrocket mass and optimized geometries will make the rocket suitable for flight, with potential accelerations reaching 25g at thrust levels of about 40 mN. For higher-thrust applications, explosive propulsion by means of sealed combustion chambers may be viable, and could potentially be used in conjunction with rocket propulsion.

7.5 Power Conversion

The temperatures can reach thousands of degrees during propellant combustion. Temperature differentials between thermally isolated areas on the rocket can be exploited to convert thermal energy into electrical energy. A convenient way of doing this is by integrating thermopiles on the silicon nozzle chip. Substantial voltages and potentially hundreds of μW of power can be used to drive on-board circuitry, or potentially control surfaces for guided microrocket flight. An order of magnitude improved thermopile performance could be achieved by using optimal thermopile materials and increasing the number of thermopiles.

7.6 Wrap-Up

This work has demonstrated the feasibility of a microrocket system designed for flight. A broad range of topics and considerations have been touched on, from propellant combustion anal-

ysis to microfabrication techniques for thermal power converters. Deeper investigation into each domain addressed should bring about significant microrocket performance improvements. The next step is performance optimization, and potentially the addition of control surfaces for guided missions.

8. References

[1] Kahn, J.M., Katz, R. H. and Pister, K. S. J., “Mobile Networking for Smart Dust,” ACM/ IEEE Intl. Conf. on Mobile Computing and Networking (MobiCom 99), Seattle, WA, August 17-19, 1999.

[2] Hsu, V., Kahn, J. M., and Pister, K. S. J., "Wireless Communications for Smart Dust," Electronics Research Laboratory Technical Memorandum Number M98/2, February, 1998.

[3] Last, M., Pister, K., "2DOF Actuated Micromirror Designed for Large DC Deflection," MOEMS 99.

[4] Atwood, B., Warneke, B., Pister, K., “Preliminary Circuits for Smart Dust,” 2000 Southwest Symposium on Mixed-Signal Design, Feb 2000.

[5] Janson, S.W., Helvajian, H., Hansen, W., Lodmell, Lt. J. “Microthrusers for nanosatellites,” Proc. MicroNanotechnology for Space Applications, Vol. 1, April 1999.

[6] Janson, S., Helavijian, H., “Batch-Fabricated Microthrusters: Initial Results,” 32nd SISS/ ASME/SAE/ASEE Joint Propulsion Conference, Lake Buena Vista, FL, 1996.

[7] Bayt, R.L., “Analysis, Fabrication, and Testing of a MEMS-Based Micropropulsion System,” Ph.D. thesis, MIT 1999.

[8] Rossi, C., *et al*, “A new generation of MEMS based Microthrusters for Microspacecraft Applications,” Proc. MicroNanotechnology for Space Applications, Vol. 1, April 1999.

[9] Musser, G. and Alpert, M., “How to Go to Mars,” Scientific American, vol. 282, No. 3. March 2000, pp. 44-51.

[10] Koeneman, P. B., Busch-Vishniac, I. J., Wood, K. L., “Feasibility of Micro Power Supplies for MEMS, Journal of Microelectromechanical Systems,” vol. 6, No. 4, Dec 1997.

[11] Sutton, G.P., Rocket Propulsion Elements, John Wiley & Sons, Inc., 1992.

[12] Purrington, G.W., Plastic Resin Bonded High Energy Rocket Fuel Systems, Firefox Enterprises, Inc. 1989.

[13] Williams, F.A., Combustion Theory, 2nd ed., Benjamin/Cummings Pub. Co., Menlo Park, CA, 1985.

[14] Kishore, K., Gayathri, V., “Chemistry of Ignition and Combustion of Ammonium-Perchlorate-Based Propellants,” Fundamentals of Solid Propellant Combustion, Chpt. 2, ed. Kuo, K.K., Summerfield, M., Prog in Astronautics and Aeronautics, vol. 90, 1984.

[15] Sigman, R. K., Price, E. W., Chakravarthy, S. R., and Zachary, E. K., “Subignition Heating Tests for Flake and Powdered Aluminum,” Proc. 3rd Annual JANNAF Combustion Meeting, Monterey, CA, CPIA, November 1996.

[16] Ayon, A., Bayt, R., Lin, C., Braff, R., Sawin, H., Schmidt, M., “Etching Characteristics and Profile Control in a Time Multiplexed Inductively Coupled Plasma Etcher,” Sensors and Actuators Workshop, Hilton Head 1998.

[17] Baltes, H., Moser, D., Freidemann, V., “Thermoelectric Microsensors and Microsystems, Mechanical Sensors,” Sensors vol. 7 ed. Bau, H.H., de Rooji, B., Kloeck, VCH Verlag,

Weinheim, pp.13-55, 1994.
[18] Van Herwaarden, A.W., Sarro, P.M., “Thermal Sensors Based on the Seebeck Effect,” Sensors and Actuators, vol. 10, nos.3&4, Nov/Dec 1986.
[19] Jaeggi, D. Thermal Converters by CMOS Technology, Ph.D. Thesis, Zurich: Physical Electronics Laboratory. 1996.
[20] Leggenhager, R., and Baltes, H., “Improved Thermoelectric Infrared Sensor Using Double Poly CMOS Technology,”Intl. Conference on Solid-State Sensors and Actuators (Transducers ‘93), pp.1008-1011, June, 1993.
[21] Muller, M. *et al*, “A Thermoelectric Infrared Radiation Sensor with Monolithically Integrated Amplifier Stage and Temperature Sensor,” Intl. Conference on Solid-State Sensors and Actuators (Transducers ‘95), pp. 640-643, June, 1995.
[22] Olgun, Z., Akar, O., Kulah, H., and Tayfun, “An Integrated Thermopile Structure with High Responsivity Using any Standard CMOS Process,” A. Intl. Conference on Solid-State Sensors and Actuators (Transducers ‘97), pp.1263-1266, June, 1997.
[23] Milanovic, V., Hopcroft,M., Zincke, C. A., Gaitan, M.,Zaghloul, M. E., Pister, K. S. J., "Modeling of Thermoelectric Effects in Planar Micromachined Structures Using SPICE," *submitted to 6th Int. Workshop on Thermal Investigations of ICs and Systems, THERMINIC'00*, May. 2000.